UNIVERSITY OF PARDUBICE
FACULTY OF CHEMICAL TECHNOLOGY
Department of General and Inorganic Chemistry

Ing. Tomáš Netolický

Photoluminescence in rare-earth ion-doped nanocrystalline oxides with garnet structure

Theses of the Doctoral Dissertation

Pardubice 2023

Study program: **Chemistry and Technology of Materials**
Study field: **Chemistry and Technology of Inorganic Materials**

Author: **Ing. Tomáš Netolický**
Supervisor: **prof. Ing. Tomáš Wágner, DrSc.**
Year of the defense: 2023

REFERENCES

Netolický, Tomáš. *Photoluminescence in rare-earth ion-doped nanocrystalline oxides with garnet structure*. Pardubice, 2023. 121 pages. Dissertation thesis (PhD.). University of Pardubice, Faculty of Chemical Technology, Department of General and Inorganic Chemistry. Supervisor prof. Ing. Tomáš Wágner, DrSc.

ABSTRACT

Presented dissertation thesis is devoted to the study of nanocrystalline oxides with garnet-related structure containing trivalent cations of rare earths. The chosen host material is $Yb_3Ga_5O_{12}$ with the use of Er^{3+} or Ho^{3+} dopants in order to achieve intense photoluminescence emission from the visible to the near-infrared region when excited by a 980nm laser. The results of the presented thesis are divided into three main parts. The first part is devoted to the study of the phase composition, structure, morphology and chemical composition of nanocrystalline oxides $Yb_{15-x}Er_xGa_{25}O_{60}$ and $Yb_{15-x}Ho_xGa_{25}O_{60}$ with $x = 0$; 0.01; 0.1; 0.5; 1 and 2. The sol-gel combustion method using citric acid as a chelating agent is chosen as the starting method for the preparation of these potential phosphors. The second part of the thesis deals with the optical properties of nanocrystalline oxides of the $Yb_{15-x}Er_xGa_{25}O_{60}$ series with a focus on photoluminescence properties. The achievement of intense Stokes photoluminescence in the near-infrared region (λ_{em} ≈1450–1650 nm) and intense anti-Stokes photoluminescence, which is dominant in the "red" region (λ_{em} ≈630–700 nm), is discussed based on the presence of efficient energy transfer (ET) $Yb^{3+} \rightarrow Er^{3+}$, energy back transfer (EBT) $Er^{3+} \rightarrow Yb^{3+}$ and cross-relaxation (CR) $Er^{3+} \leftrightarrow Er^{3+}$. The third part of the thesis deals with the optical properties of nanocrystalline oxides of the $Yb_{15-x}Ho_xGa_{25}O_{60}$ series, again focusing on photoluminescence properties. In this case, two types of intense Stokes emission spectra in the near-infrared region are achieved (λ_{em} ≈1100–1300 nm and λ_{em} ≈1800–2200 nm) together with anti-Stokes photoluminescence, where the perceived color area changes with different Ho^{3+} concentration. The ET $Yb^{3+} \rightarrow Ho^{3+}$, EBT $Ho^{3+} \rightarrow Yb^{3+}$ and CR $Ho^{3+} \leftrightarrow Ho^{3+}$ processes responsible for the observed phenomena are discussed. The detection of these processes in the both series of studied samples is possible thanks to the use of photoluminescence spectroscopy in the steady-state, time-dependent and power-dependent mode. The results of the presented thesis point to a high influence of the Er^{3+}/Ho^{3+} dopant concentration in nanocrystalline $Yb_3Ga_5O_{12}$ on the resulting photoluminescence properties with emphasis to the potential use of the studied materials.

ABSTRAKT

Předkládaná disertační práce je věnována studiu nanokrystalických oxidů granátové struktury obsahujících trojmocné kationty vzácných zemin. Zvoleným hostitelským materiálem je $Yb_3Ga_5O_{12}$ s použitím dopantů Er^{3+}, či Ho^{3+} s cílem dosažení intenzivní fotoluminiscence od viditelné až po blízkou infračervenou oblast při excitaci 980nm laserem. Výsledky předkládané práce jsou rozděleny na tři hlavní části. První část je věnována studiu fázového složení, struktury, morfologie a chemického složení nanokrystalických oxidů $Yb_{15-x}Er_xGa_{25}O_{60}$ a $Yb_{15-x}Ho_xGa_{25}O_{60}$ kde x = 0; 0,01; 0,1; 0,5; 1 a 2. Jako výchozí metoda přípravy těchto potenciálních luminoforů je zvolena sol-gel spalovací metoda s použitím kyseliny citronové jako chelatačního činidla. Druhá část práce se zabývá optickými vlastnostmi nanokrystalických oxidů řady $Yb_{15-x}Er_xGa_{25}O_{60}$ se zaměřením na fotoluminiscenční vlastnosti. Dosažení intenzivní Stokesovy fotoluminiscence v blízké infračervené oblasti ($\lambda_{em} \approx$ 1450–1650 nm) a intenzivní anti-Stokesovy fotoluminiscence, která je dominantní v „červené“ oblasti ($\lambda_{em} \approx$ 630–700 nm), je diskutováno na základě přítomnosti účinných procesů energetického přenosu (ET) $Yb^{3+} \rightarrow Er^{3+}$, zpětného energetického přenosu (EBT) $Er^{3+} \rightarrow Yb^{3+}$ a křížových relaxací (CR) $Er^{3+} \leftrightarrow Er^{3+}$. Třetí část práce se zabývá optickými vlastnostmi nanokrystalických oxidů řady $Yb_{15-x}Ho_xGa_{25}O_{60}$ opět se zaměřením na fotoluminiscenční vlastnosti. V tomto případě je dosaženo dvou typů intenzivních Stokesových emisních spekter v blízké infračervené oblasti ($\lambda_{em} \approx$ 1100–1300 nm a $\lambda_{em} \approx$ 1800–2200 nm) a anti-Stokesovy fotoluminiscence, jejíž vnímaná barevná oblast se mění s měnící se koncentrací Ho^{3+}. Jsou diskutovány procesy ET $Yb^{3+} \rightarrow Ho^{3+}$, EBT $Ho^{3+} \rightarrow Yb^{3+}$ a CR $Ho^{3+} \leftrightarrow Ho^{3+}$, zodpovědné za pozorované jevy. Odhalení těchto procesů u obou řad studovaných vzorků je možné díky využití fotoluminiscenční spektroskopie v ustáleném stavu, časově rozlišené a fotoluminiscenční spektroskopie s použitím různého excitačního výkonu. Výsledky předkládané práce poukazují na vysoký vliv koncentrace dopantu Er^{3+}/Ho^{3+} v nanokrystalickém $Yb_3Ga_5O_{12}$ na výsledné fotoluminiscenční vlastnosti s ohledem na potenciální využití studovaných materiálů.

KEYWORDS

Garnets, $Yb_3Ga_5O_{12}$, Er^{3+}, Ho^{3+}, nanocrystalline oxides, optical properties, photoluminescence, upconversion photoluminescence.

KLÍČOVÁ SLOVA

Granáty, $Yb_3Ga_5O_{12}$, Er^{3+}, Ho^{3+}, nanokrystalické oxidy, optické vlastnosti, fotoluminiscence, upkonverzní fotoluminiscence.

TABLE OF CONTENTS

1. INTRODUCTION

The study of low-dimensional inorganic materials has undergone tremendous development in the last few decades. This is due to the development of methods for their preparation and characterization as well as to a wide range of applications, e.g. in medicine, catalysis, electronics, optoelectronics, photonics, etc. Nanocrystalline oxides doped with trivalent lanthanide cations play an important role for applications based on the conversion, generation or detection of electromagnetic radiation [1, 2].

Oxides with garnet-related structure, in which a trivalent rare-earth cation occupy the dodecahedral position, appear to be a suitable host matrices for trivalent lanthanide cations. The interest in these materials began to grow with the discovery of laser oscillations in 1964 in the now commercially-available $Y_3Al_5O_{12}$ garnet doped with Nd^{3+} in single crystalline form. The reason for the constant interest in this group of materials in the both single crystalline and powder form is some of their unique properties. These properties are mainly excellent mechanical, thermal and chemical resistance and relatively low phonon energies [3–7].

Presented dissertation thesis deals with nanocrystalline $Yb_3Ga_5O_{12}$ garnet doped with Er^{3+} or Ho^{3+} ions. The theoretical part of the thesis is devoted to the basic physical, structural and chemical properties of materials with garnet-related structure and to the nanocrystalline oxides and basic methods for their synthesis from solution. The main attention in this part is paid to trivalent cations of lanthanides, 4f ↔ 4f electronic transitions of these ions and therefore the photoluminescence properties. Aspects of anti-Stokes photoluminescence, i.e. upconversion photoluminescence, are discussed in more detail. The experimental and following part is focused on the study of the structure, morphology, chemical composition and optical properties of the prepared nanocrystalline garnets. The attention in this part is paid to explain the photoluminescence properties of the prepared materials by analyzing steady-state, time-dependent and power-dependent emission spectra. The prepared materials appear to be suitable for a potential use, for example, for biological imaging, gas sensors, or infrared radiation detectors.

2. THEORETICAL PART

2.1. Materials with garnet-related structure

The family of materials with garnet-related structure refers to all materials with the general chemical formula $A_3B_2C_3X_{12}$, crystallizing mostly in a cubic lattice. "A" denotes a cation in a dodecahedral position, "B" denotes a cation in an octahedral position, "C" denotes a cation in a tetrahedral position and "X" denotes one of the anions: O^{2-}, OH^-, F^-, or a combination thereof. However, most garnets, whether occurring in nature in the form of minerals or synthetic, contain only the O^{2-} anion. We are then talking about oxide garnets with the general formula $A_3B_2C_3O_{12}$. The cubic lattice of oxide garnets is body-centered, with the space group $Ia\bar{3}d$, containing 160 atoms (8 formula units). The arrangement of atoms in the unit cell is relatively tight and the garnet structure is characterized by a high percentage of shared edges of individual polyhedrons. One can imagine the garnet structure as a continuous three-dimensional network in which each tetrahedron shares two non-adjacent edges with triangular dodecahedrons, each octahedron shares six edges with triangular dodecahedrons and each triangular dodecahedron shares four edges with surrounding triangular dodecahedrons. At the same time, tetrahedrons share vertices with octahedrons. Generally, the ionic radius r of each cation in each type of polyhedron is: $r_A > r_B > r_C$. The portion of the garnet structure is illustrated in Fig. 1 [3, 8–10].

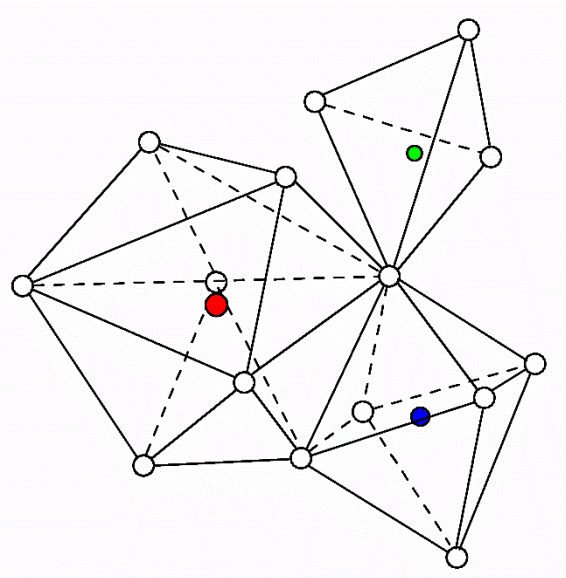

Fig. 1. Portion of the garnet structure with cations in the dodecahedral position (red circle), octahedral position (blue circle) and tetrahedral position (green circle). White circles denote O^{2-} anions.

The tolerance factor of the garnet structure can be expressed by Eq. (1):

$$\tau_f = \frac{\sqrt{(r_B + r_D)^2 - \frac{4}{9}(r_A + r_D)^2}}{2(r_C + r_D)} \quad (1)$$

where r_A, r_B, r_C and r_D denote the ionic radius of cation A, B, C and anion D, respectively. The value of τ_f for the formation of an ideal stable garnet structure is 1 [11].

The unique properties of materials with garnet-related structure include high hardness, density and refractive index along with a relatively low maximum phonon

energies. The advantage of the relatively complicated garnet structure is the possibility of incorporating other atoms (dopants) into this structure in order to control and optimize the resulting properties. Such an appropriate dopants can be rare earths, alkali metals, alkaline earth metals, transition or non-transition metals. Synthetic oxide garnets have a wide range of applications, for example solid electrolytes, magneto-optical sensors, scintillators, lasers, electroluminescent diodes, phosphors for biological imaging, etc. Monocrystalline, polycrystalline, or thin-layer samples of oxide garnets can be prepared, depending on the targeted application [4–8, 12–15].

2.1.1. $Yb_3Ga_5O_{12}$

A high phase stability with a value of $\tau_f = 0.998$ was predicted for the ytterbium gallium garnet ($Yb_3Ga_5O_{12}$), which is the focus of this work [11]. Some of the works on $Yb_3Ga_5O_{12}$ garnet were devoted to study Faraday rotation [16], paramagnetic properties [17], spin dynamics [18], dielectric properties [19], or thermophotovoltaic properties [20]. However, only a small attention was devoted to study photoluminescence in rare-earth/transition-metal doped $Yb_3Ga_5O_{12}$. V. Singh and co-authors [21] prepared Cr^{3+}-doped $Yb_3Ga_5O_{12}$ nanocrystals by solution combustion route using glycine with the resulting mean crystallite size ≈29 nm and recorded an emission spectrum in the visible region after 371nm excitation. A. Dulda [22] prepared Er^{3+}/Nd^{3+}-doped $Yb_3Ga_5O_{12}$ nanocrystals by a precipitation method with the resulting mean crystallite size up to ≈10 nm and recorded emission spectra in the visible and near-infrared regions with 805nm and 980nm excitation. Nevertheless, the photoluminescence properties of Er^{3+}-doped $Yb_3Ga_5O_{12}$ in Ref. [22] were not studied in more detail and the emission intensity was affected by a relatively small crystallite size.

2.2. Nanocrystalline oxides

Nanocrystalline oxides can be defined as materials with a particle size smaller than 100 nm, where only O^{2-} appear as anions. Compared to bulk materials, nanocrystalline materials differ in particular in high surface-to-volume ratio, but the chemical stability is still maintained. However, the high surface-to-volume ratio leads to the adsorption of some impurities, especially hydroxyl (−OH) groups on the surface of the nanocrystals. This leads to a decrease of luminescence quantum yield and to a broadening of the luminescence spectra in nanocrystalline oxides doped with lanthanides compared to bulk oxides doped with lanthanides. However, in comparison with widely studied quantum dots (e.g. CdSe), quantum confinement effects usually do not occur in nanocrystalline oxides doped with lanthanides as the particle size decreases [1, 2].

According to the principle, the synthetic methods of nanostructured materials generally can be divided into two approaches referred as “top-down” and “bottom-up”. The “top-down” approach is based on the transformation of bulk materials into nanostructured particles. It is mainly based on grinding of bulk materials, but it can also include methods such as laser ablation or sputtering. Although the methods using “top-down” approach are relatively simple, the disadvantage is the difficulty to control the resulting shape and size of the products. The “bottom-up” approach is based on individual atoms or molecules that are clustered and arranged in a controlled manner to create nanostructured particles. Compared to the “top-down” approach, the advantage of the “bottom-up” approach is the possibility significantly influence the resulting chemical composition by synthetic conditions as well as the shape and size of the

products. The “bottom-up” approach includes chemical vapor deposition methods and solution-based methods, e.g. sol-gel combustion, precipitation, co-precipitation, hydrothermal and solvothermal methods [1, 2, 23–26].

2.3. Photoluminescence

Photoluminescence is the process of emission of electromagnetic radiation from a certain substance after its excitation by another electromagnetic radiation. In the case of Stokes photoluminescence, the excitation wavelength is always shorter than the emission wavelength ($\lambda_{exc} < \lambda_{em}$; therefore $E_{exc} > E_{em}$). From the thermodynamic point of view, photoluminescence is a non-equilibrium process and therefore an excess amount of radiation is emitted than would correspond to the Plank's law. The Stokes shift, which is defined as a difference between the excitation energy and the emission energy, originates mainly from non-radiative processes of thermalization and phonon emission. If a luminescence process is spin-allowed (spin multiplicity of the excited and ground energy levels is same), one may speak about fluorescence. If a luminescence process is spin-forbidden (spin multiplicity of the excited and ground energy levels differs), one may speak about phosphorescence. The radiative lifetime for fluorescence is typically in the range of 0.1 to 10 ns, while for phosphorescence it is typically in the range of 1 ms to 10 s [27–29].

From a physical point of view, photoluminescence in inorganic semiconductors can be based on intrinsic electronic transitions between electronic bands of atoms/molecules, or on extrinsic electronic transitions of some impurities/defects. The intrinsic photoluminescence is possible only in a high-purity semiconductors. In this case, an electron is excited from the valence band to the conduction band and a vacancy created in the valence band than undergoes radiative recombination together with the excited electron. However, the extrinsic photoluminescence can occur only in semiconductors with some admixture – an activator (dopant) or structure defects. Paramagnetic ions of transition metals or of rare earths are the most common dopants in inorganic materials. The emission bands of paramagnetic ions of transition metals originate from d ↔ d electronic transitions of partially filled d orbitals. The emission bands of paramagnetic ions of rare earths originate mostly from 4f ↔ 4f electronic transitions of partially filled f orbitals. Although neither the d ↔ d nor the 4f ↔ 4f electronic transitions are generally allowed in terms of selection rules, the realization is possible due to an influence of the surrounding ligand field. The emission wavelength of the paramagnetic ions from the 4th period can change significantly due to the influence of different host matrix, since the relatively large 3d orbitals are not so effectively shielded by electron from the outer shells. However, the emission wavelength of the paramagnetic lanthanide ions does not change significantly in different host matrices. This is due to the presence of relatively small 4f orbitals inside the larger shells, which makes the 4f orbitals less sensitive to the surrounding ligand field. Sensitizers are often being used as dopants together with photoluminescence activators. The purpose of the sensitizer is absorption of the excitation radiation and efficient energy transfer from the sensitizer to the activator [27–29].

2.4. Upconversion photoluminescence

Upconversion photoluminescence (UCPL) is a non-linear type of photoluminescence that does not obey the Stokes' law and therefore belongs to an anti-Stokes processes. UCPL is based on the emission of electromagnetic radiation of a shorter wavelength than the wavelength of the excitation radiation ($\lambda_{exc} > \lambda_{em}$; therefore $E_{exc} < E_{em}$). The generation of photons with a shorter wavelength compared to photons of excitation radiation involves the successive absorption of two or more photons or energy transfer taking place at the real metastable excited energy levels of one or more ions. Lanthanide ions (Ln^{3+}) are used most often as UCPL activators, e.g. Pr^{3+}, Nd^{3+}, Ho^{3+}, Er^{3+} and Tm^{3+}. The UCPL phenomenon was also observed when using some transition metal cations, e.g. Ti^{2+}, Ni^{2+} and Mo^{3+}. The host matrices can be in various forms, e.g. single crystals, optical fibers, glasses, thin films, or powders. The UCPL phenomenon is currently used for the construction of continuous fiber lasers, fiber amplifiers, layers for increment of quantum efficiency of solar cells, or for the phosphors for biological imaging. The non-linear optical phenomenon opposite to UCPL is photon downconversion. In photon downconversion, one photon is absorbed while two or more photons of lower energy are emitted. Although there are four main UCPL mechanisms within Ln^{3+}, the following attention will be paid to two of them, which are important for this work [28, 30–33].

2.4.1. Ground state absorption/excited state absorption

The ground state absorption followed by the excited state absorption (GSA/ESA) is the simplest UCPL mechanism. The principle of the GSA/ESA mechanism is shown in Fig. 2 for the Er^{3+} ion. By absorbing an excitation radiation of λ_{exc} ≈980 nm, the electron is transferred from the ground energy level $^4I_{15/2}$ to the $^4I_{11/2}$ level. By another absorption of this excitation radiation, the electron is transferred from the excited energy level $^4I_{11/2}$ to the $^4F_{7/2}$ level. The $^4F_{7/2}$ level is thermally coupled to the $^2H_{11/2}$ and $^4S_{3/2}$ manifolds, thus resulting in the multiphonon relaxation (MPR) to the $^4S_{3/2}$ level. The following radiative transition $^4S_{3/2} \rightarrow {}^4I_{15/2}$ is associated with the release of radiation of λ_{em} ≈550 nm. The GSA/ESA mechanism takes place within a single ion and is almost independent of the UCPL ion concentration [28, 30, 32].

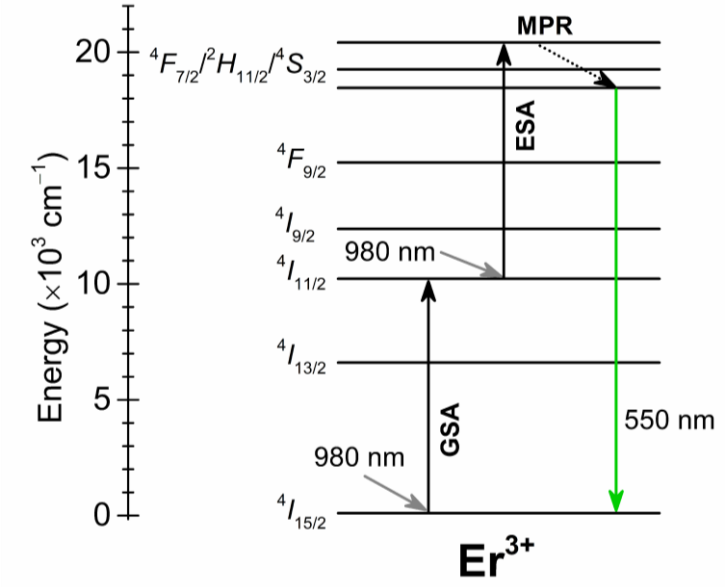

Fig. 2. General principle of the GSA/ESA UCPL mechanism for the Er^{3+} ion using an excitation radiation source of λ_{exc} ≈980 nm.

2.4.2. Energy transfer upconversion

The energy transfer upconversion (ETU) mechanism requires the presence of at least two optically active ions. The ETU mechanism is therefore strongly dependent on the interionic distance and thus on the ion concentration. The ETU mechanism can be divided into two types – ETU occurring within one type of ion and ETU occurring within two ion types. In both cases, however, one ion acts as a sensitizer and the other ion acts as an activator. However, the energy of at least one metastable (excited) level of both ions must be similar (thus in resonance). The principle of the ETU mechanism is shown in Fig. 3 for the Er^{3+} and Yb^{3+} ions. The excited $^2F_{5/2}$ level of the Yb^{3+} sensitizer ion is populated via the GSA process. The absorbed energy is subsequently transferred by the ET1 process to the metastable level $^4I_{11/2}$ of the neighboring Er^{3+} ion. Another GSA process at the Yb^{3+} ion is followed by the ET2 process to the Er^{3+}: $^4F_{7/2}$ level. After the MPR process to the $^4S_{3/2}$ level, the emission of radiation of λ_{em} ≈550 nm occurs by recombination: Er^{3+}: $^4S_{3/2} \rightarrow {}^4I_{15/2}$. However, the Er^{3+} ion can also be excited to the $^4I_{11/2}$ level by the GSA process, and then only the ET2 process would take place. The Yb^{3+} ions are being widely used as co-dopants together with the Er^{3+} ions. It results in a high efficiency of the $Yb^{3+} \rightarrow Er^{3+}$ energy transfer and thus in a higher intensity of the UCPL emission spectra compared when using only the Er^{3+} ions. However, finding the appropriate Yb^{3+}/Er^{3+} doping ratio is very important [28, 30, 32, 34].

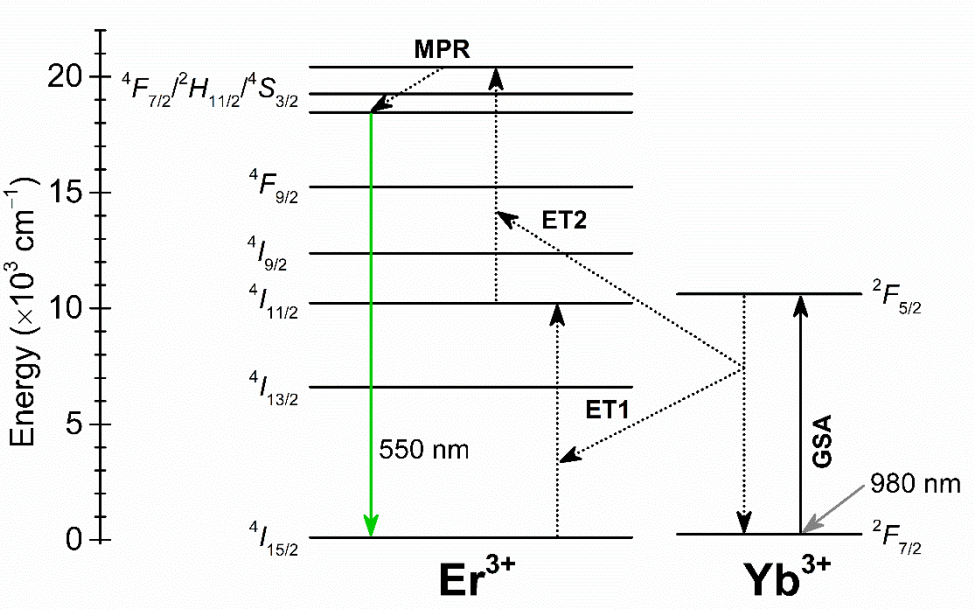

Fig. 3. General principle of the ETU UCPL mechanism for the Er^{3+} and Yb^{3+} ions using an excitation radiation source of λ_{exc} ≈980 nm.

3. EXPERIMENTAL PART

The garnet nanocrystals of composition $Yb_3Ga_5O_{12}$, $Yb_{14,99}Er_{0,01}Ga_{25}O_{60}$, $Yb_{14,9}Er_{0,1}Ga_{25}O_{60}$, $Yb_{14,5}Er_{0,5}Ga_{25}O_{60}$, $Yb_{14}Er_1Ga_{25}O_{60}$, $Yb_{13}Er_2Ga_{25}O_{60}$, $Yb_{14,99}Ho_{0,01}Ga_{25}O_{60}$, $Yb_{14,9}Ho_{0,1}Ga_{25}O_{60}$, $Yb_{14,5}Ho_{0,5}Ga_{25}O_{60}$, $Yb_{14}Ho_1Ga_{25}O_{60}$ and $Yb_{13}Ho_2Ga_{25}O_{60}$ were prepared using a sol-gel combustion technique. The starting chemicals were Ga (5N), Yb_2O_3 (3N) and Er_2O_3 (4N) or Ho_2O_3 (3N). These were weighed at a total batch of 1 g of the resulting products. These were then dissolved in high-purity HNO_3 and the excess HNO_3 was subsequently removed at 90°C. The dried metal nitrates were then dissolved in 50 ml of deionized water. The metal nitrates in water solution were chelated by citric acid keeping the molar ratio of citric acid to metals (Ga + Yb + Er/Ho) 2.5:1. The pH of the stirred solution was subsequently set to pH ≈8 (at room temperature) by dropwise addition of highly-pure ammonia solution. The obtained solution was heated at 90°C under rigorous stirring to obtain a homogenous transparent-to-pink gel. The dried gel was decomposed in a furnace at 800°C for 2 h and subsequently at 1000°C for 30 min. The white to slightly pink powder product was then characterized by a various methods.

The crystalline structure and phase purity were investigated by X-ray diffractometer (XRD) Bruker D8 ADVANCE in the Bragg-Brentano geometry equipped with Cu $K\alpha$ radiation source. The range of the 2θ angle was from 5° to 90°. The mean crystallite size was determined with the use of Scherrer equation (2):

$$D = \frac{K\,\lambda}{\beta_{hkl}\,\cos\theta_{hkl}} \tag{2}$$

where K denotes the Scherrer constant, λ denotes the X-ray wavelength, β_{hkl} denotes the line broadening and θ_{hkl} stands for the angle of diffraction [35].

The crystalline structure was studied in more detail by attenuated total reflectance-Fourier transform infrared spectroscopy (ATR-FTIR). The infrared lattice spectra were measured using a Bruker VERTEX 70v instrument in the range from 800 to 50 cm^{-1}.

The chemical composition was studied by an Energy-dispersive X-ray (EDX) spectrometer AZtec X-Max 20 (Oxford Instruments) with accelerating voltage 20 kV. The EDX instrument was attached to a LYRA 3 scanning electron microscope (SEM), which was used for investigation of morphology.

The optical reflectivity was studied using a UV-Vis-NIR spectrophotometer JASCO V-570. The diffuse reflectance spectra were recorded in the range from 200 to 1800 nm.

The photoluminescence properties were investigated with the use of two types of instruments. The Stokes and anti-Stokes steady-state and time-dependent emission spectra of Er^{3+}-doped nanocrystals were studied together with the anti-Stokes steady-state and time-dependent emission spectra of Ho^{3+}-doped nanocrystals using an instrument FLS1000 (Edinburgh Instruments) with λ_{exc} ≈977 nm. The Stokes steady-state and time-dependent emission spectra of Ho^{3+}-doped nanocrystals were studied using a photoluminescence spectroscope equipped with a SDL-1 monochromator and with λ_{exc} ≈980 nm.

4. RESULTS AND DISCUSSION

4.1. General

Fig. 4 shows the XRD patterns of prepared $Yb_{15-x}Er_xGa_{25}O_{60}$ (a) and $Yb_{15-x}Ho_xGa_{25}O_{60}$ (b) nanocrystalline samples (x = 0, 0.01, 0.1, 0.5, 1 and 2 at.%). The XRD patterns confirm that all the prepared samples are single-phase cubic garnets corresponding to the $Yb_3Ga_5O_{12}$ structure with the space group $Ia\bar{3}d$. The mean crystallite size of the prepared samples ranges from ≈27 to ≈37 nm.

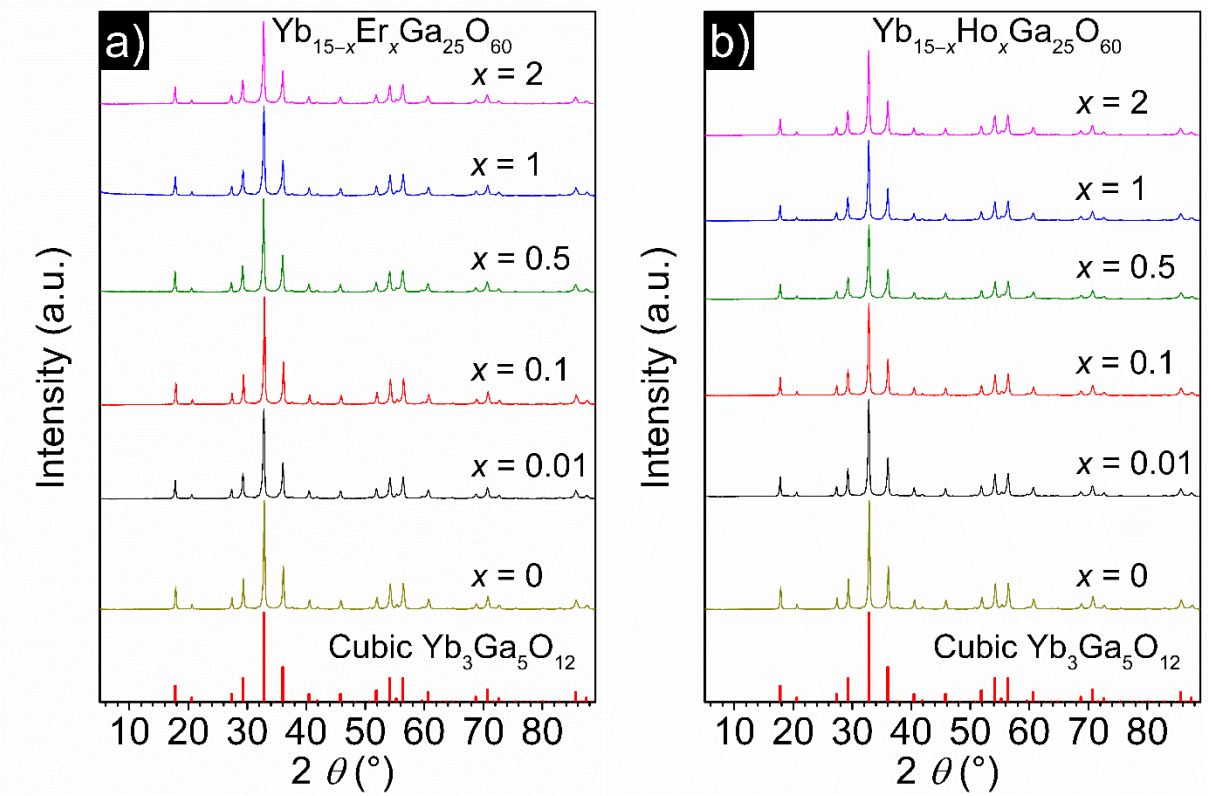

Fig. 4. Powder XRD patterns of prepared $Yb_{15-x}Er_xGa_{25}O_{60}$ (a) and $Yb_{15-x}Ho_xGa_{25}O_{60}$ (b) nanocrystalline garnets. The bottom line corresponds to the $Yb_3Ga_5O_{12}$ standard.

Fig. 5 presents the ATR spectra of prepared $Yb_{15-x}Er_xGa_{25}O_{60}$ (a) and $Yb_{15-x}Ho_xGa_{25}O_{60}$ (b) nanocrystalline garnets. The ATR spectra of all studied garnets are very similar to each other and contain absorption bands corresponding to almost same wavenumbers for each sample. The assignment of the individual absorption bands to individual structural units is based on Refs. [36–40]. The bands at ≈705 and ≈660 cm^{-1}, present as a shoulder, together with the bands at ≈635 and ≈595 cm^{-1} are assigned to the asymmetric stretching modes (ν_3) of the GaO_4 tetrahedra. The band at ≈480 cm^{-1} is assigned to a combination of the ν_3 modes of the GaO_4 tetrahedra and GaO_6 octahedra. The band at ≈450 cm^{-1}, present as a shoulder, is assigned to the ν_3 modes of the GaO_6 octahedra. The bands at ≈365, ≈305, ≈255 and ≈220 cm^{-1} represent a combination of 4 contributions: rotations of the GaO_4 tetrahedra, asymmetric bending modes (ν_4) of the GaO_4 tetrahedra, translations of the GaO_6 octahedra and ν_4 modes of the GaO_6 octahedra. The bands at ≈200 and ≈140 cm^{-1} are assigned to translations of the YbO_8 dodecahedra. The bands at ≈110 and ≈105 cm^{-1} represent a combination of translations of the GaO_4, GaO_6 and YbO_8 polyhedra. No absorption bands related to isolated Er/Ho-based structural units were observed.

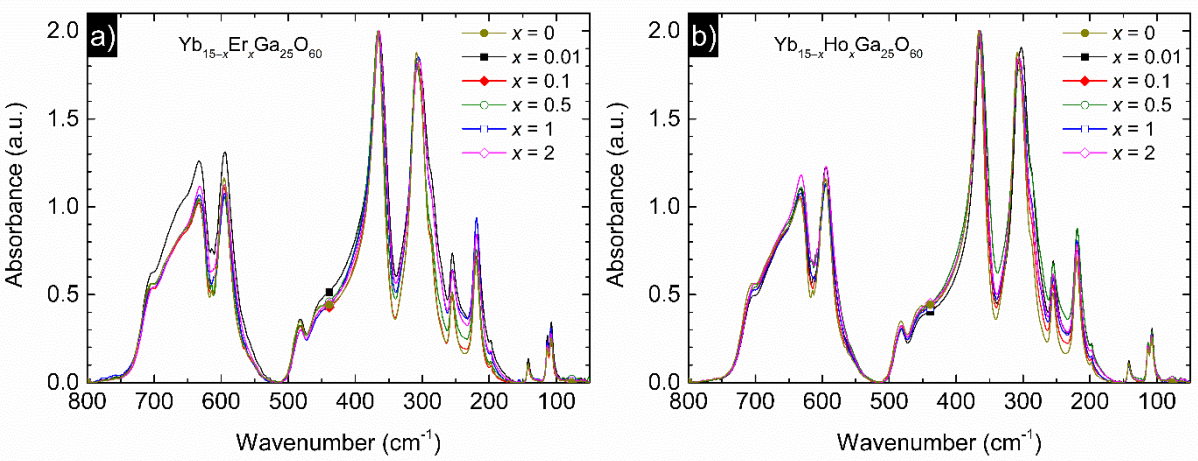

Fig. 5. ATR spectra of prepared $Yb_{15-x}Er_xGa_{25}O_{60}$ (a) and $Yb_{15-x}Ho_xGa_{25}O_{60}$ (b) nanocrystalline garnets. The spectra are normalized on the most intense band at ≈365 cm^{-1}.

Fig. 6 presents SEM image of representative $Yb_{14.5}Er_{0.5}Ga_{25}O_{60}$ sample. The sample is highly porous and is formed by many agglomerates which is a typical feature for nanocrystalline materials prepared by sol-gel combustion technique using citric acid [25].

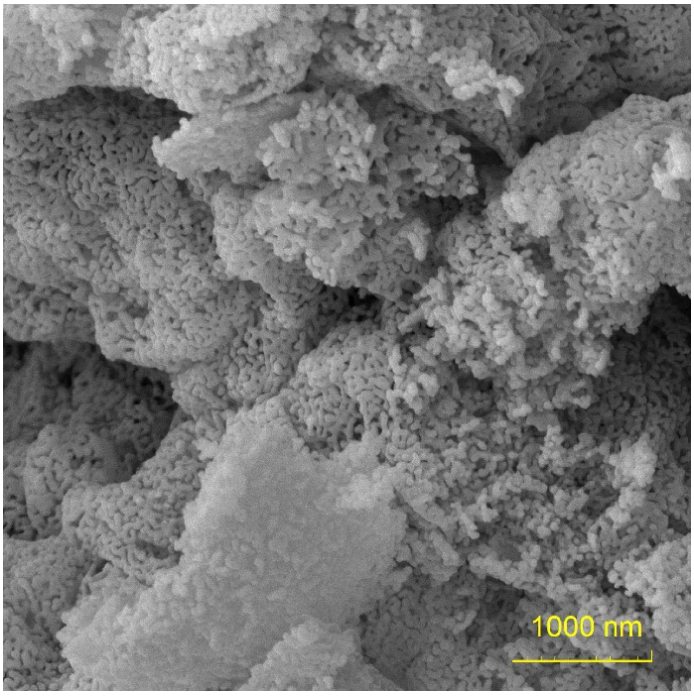

Fig. 6. SEM image of $Yb_{14.5}Er_{0.5}Ga_{25}O_{60}$ nanocrystalline sample. The scale is 1000 nm.

Tab. 1 lists the determined chemical composition of prepared $Yb_{15-x}Er_xGa_{25}O_{60}$ nanocrystalline garnets with x = 0, 0.01, 0.1, 0.5, 1 and 2. Tab. 2 lists the determined chemical composition of prepared $Yb_{15-x}Ho_xGa_{25}O_{60}$ nanocrystalline garnets with x = 0.01, 0.1, 0.5, 1 and 2. Taking into account the possible measurement error (≈±1 at.%), one can say that all the prepared samples show good conformity of the theoretical and determined chemical composition.

Tab. 1. Theoretical and EDX-determined chemical composition of $Yb_{15-x}Er_xGa_{25}O_{60}$ nanocrystalline garnets.

x		Yb (at.%)	Er (at.%)	Ga (at.%)	O (at.%)
0	Theoretical composition	15	0	25	60
	Determined composition	15.8	–	24.7	59.5
0.01	Theoretical composition	14.99	0.01	25	60
	Determined composition	16.1	–	25.3	58.6
0.1	Theoretical composition	14.9	0.1	25	60
	Determined composition	14.9	–	25.0	60.1
0.5	Theoretical composition	14.5	0.5	25	60
	Determined composition	16.0	0.5	25.5	58.0
1	Theoretical composition	14.0	1.0	25	60
	Determined composition	15.8	1.1	25.5	57.6
2	Theoretical composition	13.0	2.0	25	60
	Determined composition	13.8	2.1	25.3	58.8

Tab. 2. Theoretical and EDX-determined chemical composition of $Yb_{15-x}Ho_xGa_{25}O_{60}$ nanocrystalline garnets.

x		Yb (at.%)	Ho (at.%)	Ga (at.%)	O (at.%)
0.01	Theoretical composition	14.99	0.01	25	60
	Determined composition	15.8	–	24.6	59.6
0.1	Theoretical composition	14.9	0.1	25	60
	Determined composition	16.7	–	25.7	57.6
0.5	Theoretical composition	14.5	0.5	25	60
	Determined composition	16.6	0.6	24.4	58.4
1	Theoretical composition	14.0	1.0	25	60
	Determined composition	14.2	1.0	24.3	60.5
2	Theoretical composition	13.0	2.0	25	60
	Determined composition	13.3	2.0	24.6	60.1

4.2. Optical properties of Er^{3+}-doped $Yb_3Ga_5O_{12}$ nanocrystals

The diffuse reflectance spectra of prepared $Yb_{15-x}Er_xGa_{25}O_{60}$ nanocrystalline garnets from Fig. 7 reveal high optical reflectivity of these samples with various absorption bands. The broad and strong absorption band at ≈925 nm corresponds to GSA transition of Yb^{3+} from the $^2F_{7/2}$ ground level to the $^2F_{5/2}$ excited level. This strong absorption band is caused by high Yb^{3+} content in all samples and it overlaps the absorption band corresponding to GSA transition of Er^{3+} from the $^4I_{15/2}$ ground level to the $^4I_{11/2}$ excited level. The absorption bands centered at ≈1500, ≈800, ≈655, ≈545, ≈520, ≈490, ≈450,

≈410 and ≈375 nm are attributed to the GSA transitions of Er^{3+} from the $^4I_{15/2}$ ground level to the excited levels $^4I_{13/2}$, $^4I_{9/2}$, $^4F_{9/2}$, $^4S_{3/2}$, $^2H_{11/2}$, $^4F_{7/2}$, $^4F_{5/2}/^4F_{3/2}$, $^2G_{9/2}$ and $^4G_{11/2}$, respectively. A fundamental absorption by the $Yb_3Ga_5O_{12}$ host is present at λ <300 nm.

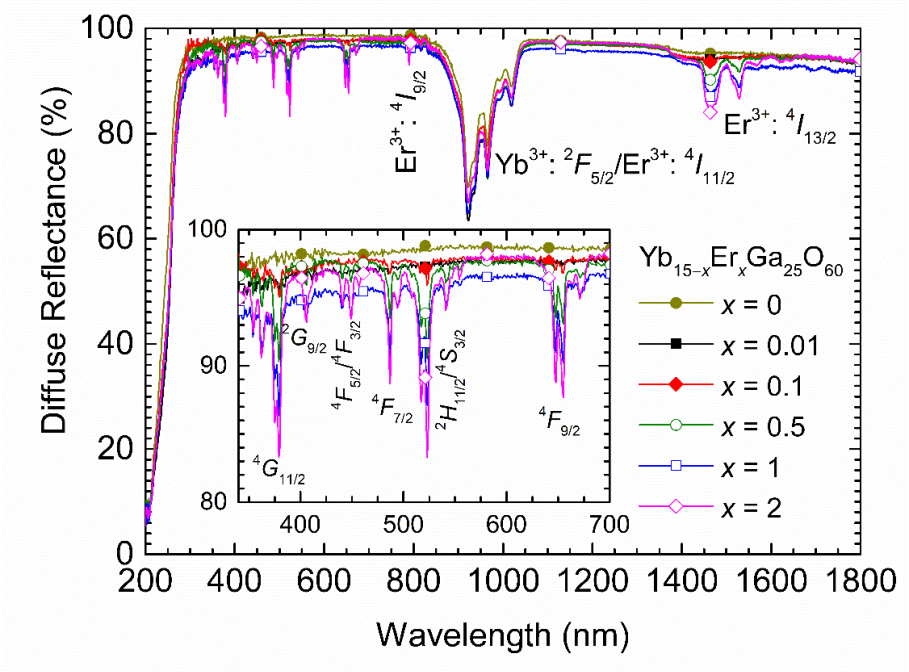

Fig. 7. Diffuse reflectance spectra of $Yb_{15-x}Er_xGa_{25}O_{60}$ nanocrystalline garnets. Inset shows detail of the spectra in the 340–700 nm region.

Fig. 8 presents the Stokes emission spectra in the near-infrared region of prepared $Yb_{15-x}Er_xGa_{25}O_{60}$ nanocrystalline garnets. The emission spectra from the graph come from the Er^{3+}: $^4I_{13/2} \rightarrow {}^4I_{15/2}$ electronic transition. However, the broadband emission from the inset of Fig. 8 was interestingly observed in the undoped $Yb_3Ga_5O_{12}$ sample. The nature of this emission was further studied in the appendix of the dissertation thesis. A relatively low emission intensity in the $Yb_{13}Er_2Ga_{25}O_{60}$ sample from Fig. 8 may be attributed to the concentration quenching effect [41, 42].

Fig. 9 presents the anti-Stokes emission (upconversion) spectra in the visible region of prepared $Yb_{15-x}Er_xGa_{25}O_{60}$ nanocrystalline garnets. The dominant emission bands are situated in "red" region (λ_{em} ≈630–700 nm) and are attributed to the Er^{3+}: $^4F_{9/2} \rightarrow {}^4I_{15/2}$ electronic transition. The inset of Fig. 9 shows a significantly less intense emission bands in "green" and "blue" regions. These are attributed to the Er^{3+}: $^4F_{7/2}/^2H_{11/2}/^4S_{3/2} \rightarrow {}^4I_{15/2}$ (λ_{em} ≈490–570 nm) and Er^{3+}: $^2G_{9/2} \rightarrow {}^4I_{15/2}$ (λ_{em} ≈410 nm) electronic transitions. The highest photoluminescence intensity was detected in the $Yb_{14.5}Er_{0.5}Ga_{25}O_{60}$ and $Yb_{14}Er_1Ga_{25}O_{60}$ samples as for the Stokes photoluminescence while again in the $Yb_{13}Er_2Ga_{25}O_{60}$ sample the concentration quenching of upconversion also occurs [41, 42].

Fig. 10 shows the CIE 1931 chromaticity diagram of the observed anti-Stokes emission in $Yb_{15-x}Er_xGa_{25}O_{60}$ nanocrystalline garnets. According to the observed diagram, the anti-Stokes emission of all prepared $Yb_{15-x}Er_xGa_{25}O_{60}$ samples occurs in a deep red region.

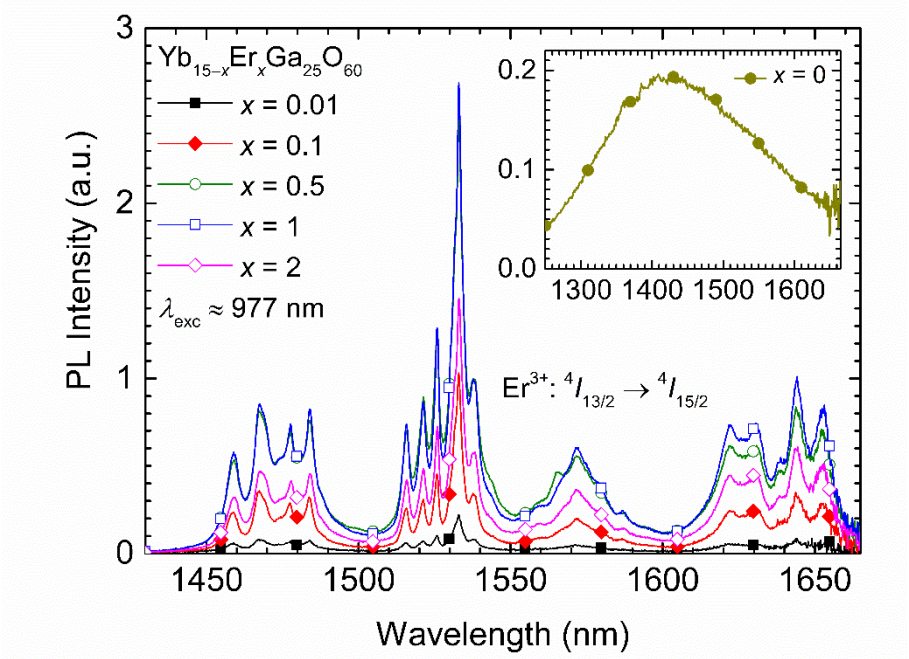

Fig. 8. Stokes Er^{3+}: $^4I_{13/2} \rightarrow {}^4I_{15/2}$ emission spectra of $Yb_{15-x}Er_xGa_{25}O_{60}$ nanocrystalline garnets. Inset shows the broadband emission in the undoped $Yb_3Ga_5O_{12}$ sample. Measured at λ_{exc} ≈977 nm.

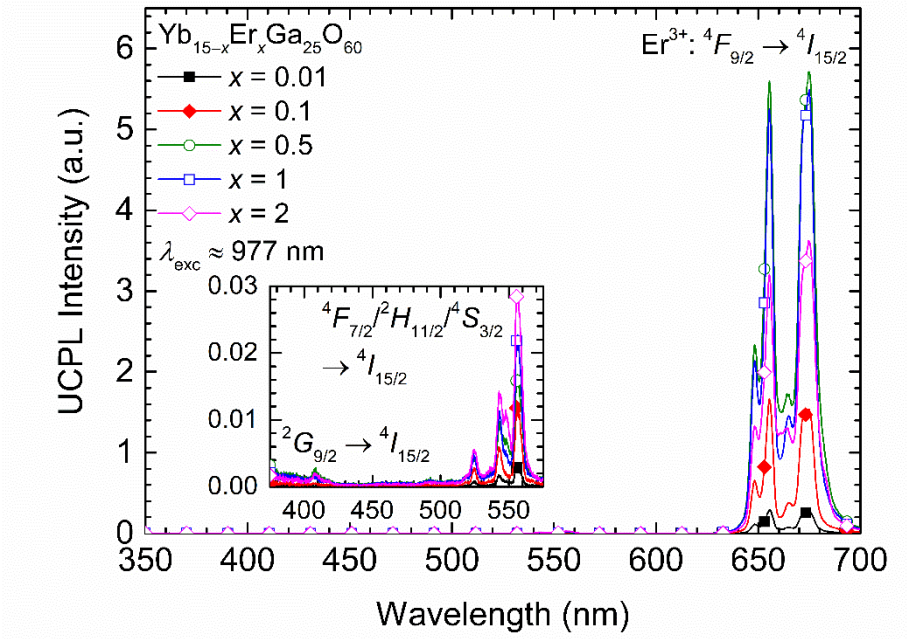

Fig. 9. Anti-Stokes emission spectra of $Yb_{15-x}Er_xGa_{25}O_{60}$ nanocrystalline garnets. Inset shows detail of the spectra in the 375–575 nm region. Measured at λ_{exc} ≈977 nm.

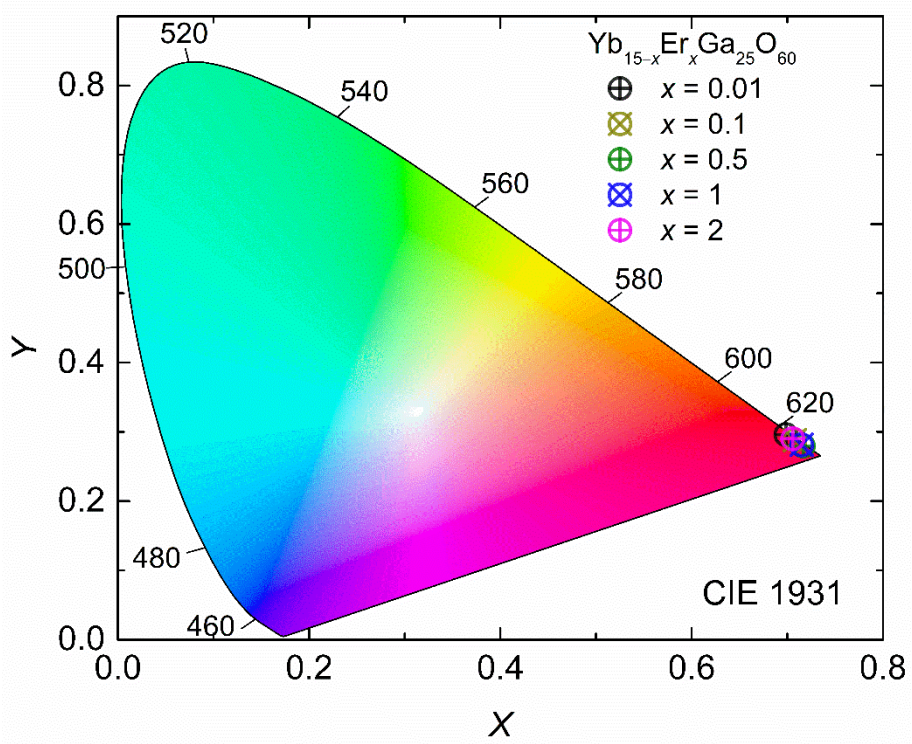

Fig. 10. CIE 1931 chromaticity diagram of the anti-Stokes emission in $Yb_{15-x}Er_xGa_{25}O_{60}$ nanocrystalline garnets.

Tab. 3 lists the determined lifetime values of radiative transitions observed in $Yb_{15-x}Er_xGa_{25}O_{60}$ nanocrystalline garnets. The short lifetime component $\tau_1(^4I_{13/2})$ is likely caused by the optically-active centers which cause the observed broadband emission in the undoped $Yb_3Ga_5O_{12}$ sample. The $\tau_1(^4I_{13/2})$ values do not significantly change with increasing Er^{3+} content. The long lifetime component $\tau_2(^4I_{13/2})$, on the other hand, is much more sensitive to the Er^{3+} content and comes directly from the Er^{3+}: $^4I_{13/2} \rightarrow {}^4I_{15/2}$ transition. The increase of $\tau_2(^4I_{13/2})$ from ≈10.35 ms ($Yb_{14.99}Er_{0.01}Ga_{25}O_{60}$ sample) to ≈11.34 ms ($Yb_{14.9}Er_{0.1}Ga_{25}O_{60}$ sample) may be caused by a radiation trapping effect [43]. The following decrease of $\tau_2(^4I_{13/2})$ up to ≈2.69 ms ($Yb_{13}Er_2Ga_{25}O_{60}$ sample) is caused by $Er^{3+} \leftrightarrow Er^{3+}$ and $Yb^{3+} \rightarrow Er^{3+}$ energy transfer processes as well as by concentration quenching effect [41, 42].

The single lifetime component $\tau_{Yb}(^2F_{5/2})$ shows very low values. It can be attributed to a high Yb^{3+} content which quenches the Yb^{3+}: $^2F_{5/2} \rightarrow {}^2F_{7/2}$ radiative transition in all studied $Yb_{15-x}Er_xGa_{25}O_{60}$ nanocrystalline garnets [41, 42]. The gradual decrease of $\tau_{Yb}(^2F_{5/2})$ values with increasing Er^{3+} content can be attributed to an increment of efficiency of the $Yb^{3+} \rightarrow Er^{3+}$ energy transfer process.

The two lifetime components $\tau_3(^4F_{9/2})$ and $\tau_4(^4F_{9/2})$ were determined in the $Yb_{14.99}Er_{0.01}Ga_{25}O_{60}$, $Yb_{14.9}Er_{0.1}Ga_{25}O_{60}$ and $Yb_{14.5}Er_{0.5}Ga_{25}O_{60}$ samples. The presence of only one lifetime component $\tau_3(^4F_{9/2})$, or $\tau_4(^4F_{9/2})$ in the $Yb_{14}Er_1Ga_{25}O_{60}$ and $Yb_{13}Er_2Ga_{25}O_{60}$ samples is caused by decrease of one of the components bellow the detection limit. However, the gradual decrease of both lifetime components as well as of the average lifetime $<\tau>(^4F_{9/2})$ with increasing Er^{3+} content from 0.01 at.% to 0.5 at.% is caused by an increment of efficiency of the $Yb^{3+} \rightarrow Er^{3+}$ energy transfer process.

Tab. 3. Lifetime values of the Stokes emission Er^{3+}: $^4I_{13/2} \rightarrow {}^4I_{15/2}$ {$\tau_1(^4I_{13/2})$ and $\tau_2(^4I_{13/2})$}, Stokes emission Yb^{3+}: $^2F_{5/2} \rightarrow {}^2F_{7/2}$ {$\tau_{Yb}(^2F_{5/2})$} and anti-Stokes emission Er^{3+}: $^4F_{9/2} \rightarrow {}^4I_{15/2}$ {$\tau_3(^4F_{9/2})$ and $\tau_4(^4F_{9/2})$}. $<\tau>(^4F_{9/2})$ is the average lifetime of the anti-Stokes emission Er^{3+}: $^4F_{9/2} \rightarrow {}^4I_{15/2}$.

x (at.%)	τ_1 ($^4I_{13/2}$) (ms)	τ_2 ($^4I_{13/2}$) (ms)	τ_{Yb} ($^2F_{5/2}$) (μs)	τ_3 ($^4F_{9/2}$) (μs)	τ_4 ($^4F_{9/2}$) (μs)	$<\tau>$ ($^4F_{9/2}$) (μs)
0	0.945±0.03	–	19±1	–	–	–
0.01	0.87±0.02	10.35±0.06	17±1	15±1	54±2	16±1
0.1	0.80±0.02	11.34±0.05	15±1	15±1	32±1	16±1
0.5	0.73±0.03	6.86±0.04	8±1	12±1	22±2	12±1
1	0.86±0.03	5.04±0.04	7±1	12±1	12±1	–
2	0.63±0.02	2.69±0.03	7±1	12±1	12±1	–

4.2.1. Photoluminescence mechanism in Er^{3+}-doped $Yb_3Ga_5O_{12}$ nanocrystals

Fig. 11 presents the proposed photoluminescence mechanism in $Yb_{15-x}Er_xGa_{25}O_{60}$ nanocrystalline garnets using $\lambda_{exc} \approx 977$ nm. Firstly, the GSA processes occur simultaneously at Er^{3+} and Yb^{3+} ions, i.e. Er^{3+}: $^4I_{15/2} \rightarrow {}^4I_{11/2}$ and Yb^{3+}: $^2F_{7/2} \rightarrow {}^2F_{5/2}$. Since the Yb^{3+}/Er^{3+} ratio is high in all studied garnets, the GSA and subsequent ESA processes within Er^{3+} ions play a negligible role. The GSA process within the Yb^{3+} ions is followed by the ETU0 process: Yb^{3+}: $^2F_{5/2}$ + Er^{3+}: $^4I_{15/2} \rightarrow Yb^{3+}$: $^2F_{7/2}$ + Er^{3+}: $^4I_{11/2}$. Absorption of another photon by the Yb^{3+} leads to the ETU1 process: Yb^{3+}: $^2F_{5/2}$ + Er^{3+}: $^4I_{11/2} \rightarrow Yb^{3+}$: $^2F_{7/2}$ + Er^{3+}: $^4F_{7/2}$. The radiative transition Er^{3+}: $^4F_{7/2}/^2H_{11/2}/^4S_{3/2} \rightarrow {}^4I_{15/2}$ is observed as a weak anti-Stokes emission band in "green" region. The intense anti-Stokes emission band in "red" region is caused by the radiative transition Er^{3+}: $^4F_{9/2} \rightarrow {}^4I_{15/2}$. The efficient depopulation of the energy levels Er^{3+}: $^4F_{7/2}/^2H_{11/2}/^4S_{3/2}$ is provided by a presence of cross-relaxation (CR) and energy back transfer (EBT) processes. The CR1 process between pairs of Er^{3+} ions is following: $^4F_{7/2}$ + $^4I_{11/2} \rightarrow {}^4F_{9/2}$ + $^4F_{9/2}$ [44, 45]. The CR2 process between pairs of Er^{3+} ions occurs as follows: $^2H_{11/2}$ + $^4I_{15/2} \rightarrow {}^4I_{9/2}$ + $^4I_{13/2}$ [44, 46]. The EBT1 process between Yb^{3+} and Er^{3+} ions is following: Er^{3+}: $^4S_{3/2}$ + Yb^{3+}: $^2F_{7/2} \rightarrow Er^{3+}$: $^4I_{13/2}$ + Yb^{3+}: $^2F_{5/2}$ [41, 47–50]. The EBT2 process may also occur: Er^{3+}: $^4F_{7/2}$ + Yb^{3+}: $^2F_{7/2} \rightarrow Er^{3+}$: $^4I_{11/2}$ + Yb^{3+}: $^2F_{5/2}$ [51]. Since the Stokes emission spectra at ≈1.5 μm come from the Er^{3+}: $^4I_{13/2} \rightarrow {}^4I_{15/2}$ transition, the multiphonon relaxation (MPR) will occur from the $^4I_{11/2}$ to the $^4I_{13/2}$ energy level. The MPR process can also contribute in population of the Er^{3+}: $^4F_{7/2}/^2H_{11/2}/^4S_{3/2}$ energy levels from higher manifolds. At the Er^{3+}: $^4I_{13/2}$ level, the ETU2 process occurs: Yb^{3+}: $^2F_{5/2}$ + Er^{3+}: $^4I_{13/2} \rightarrow Yb^{3+}$: $^2F_{7/2}$ + Er^{3+}: $^4F_{9/2}$. The ETU2 efficiency is assumed to be high due to high intensity of the anti-Stokes emission band in "red" region. Since the relatively weak anti-Stokes emission band in "blue" region was observed, the ETU3 process is also present: Yb^{3+}: $^2F_{5/2}$ + Er^{3+}: $^4F_{9/2} \rightarrow Yb^{3+}$: $^2F_{7/2}$ + Er^{3+}: $^2G_{9/2}$.

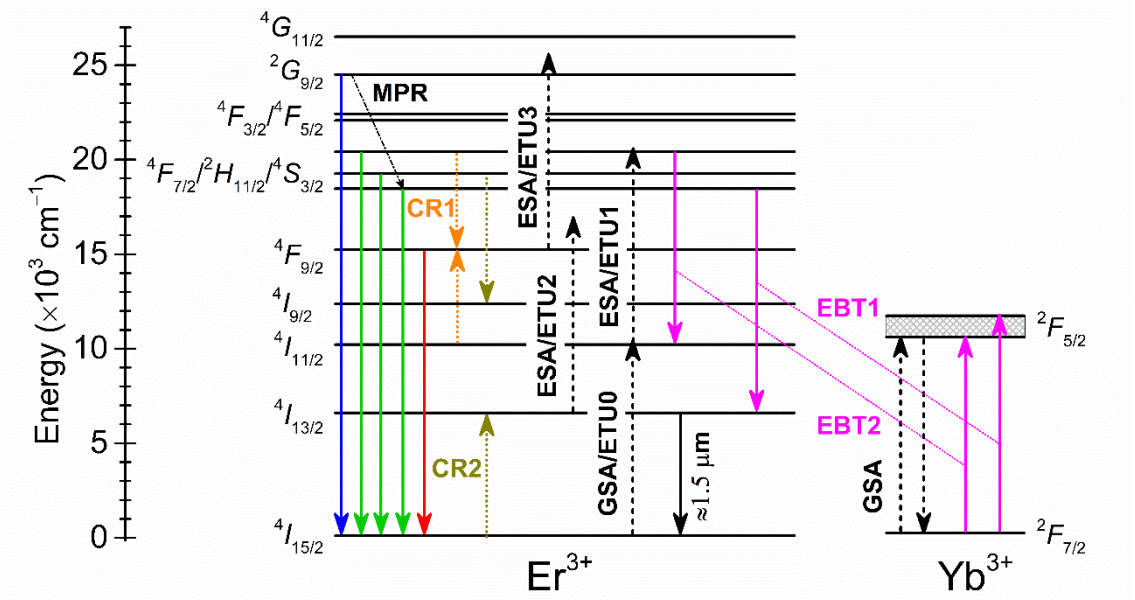

Fig. 11. Proposed photoluminescence mechanism in $Yb_{15-x}Er_xGa_{25}O_{60}$ nanocrystalline garnets using λ_{exc} ≈977 nm.

4.3. Optical properties of Ho^{3+}-doped $Yb_3Ga_5O_{12}$ nanocrystals

The diffuse reflectance spectra of prepared $Yb_{15-x}Ho_xGa_{25}O_{60}$ nanocrystalline garnets are shown in Fig. 12. The spectra show high optical reflectivity of these samples with the intense absorption band at ≈925 nm corresponding to high Yb^{3+} content as in the $Yb_{15-x}Er_xGa_{25}O_{60}$ nanocrystalline garnets. The absorption bands centered at ≈1130, ≈640, ≈535, ≈485, ≈450, ≈415 and ≈365 nm are attributed to the GSA transitions of Ho^{3+} from the $^5I_8$ ground level to the excited levels $^5I_6$, $^5F_5$, $^5F_4/^5S_2$, $^5F_3/^5F_2/^3K_8$, $^5F_1/^5G_6$, $^5G_5$ and $^3H_6/^3H_5$, respectively.

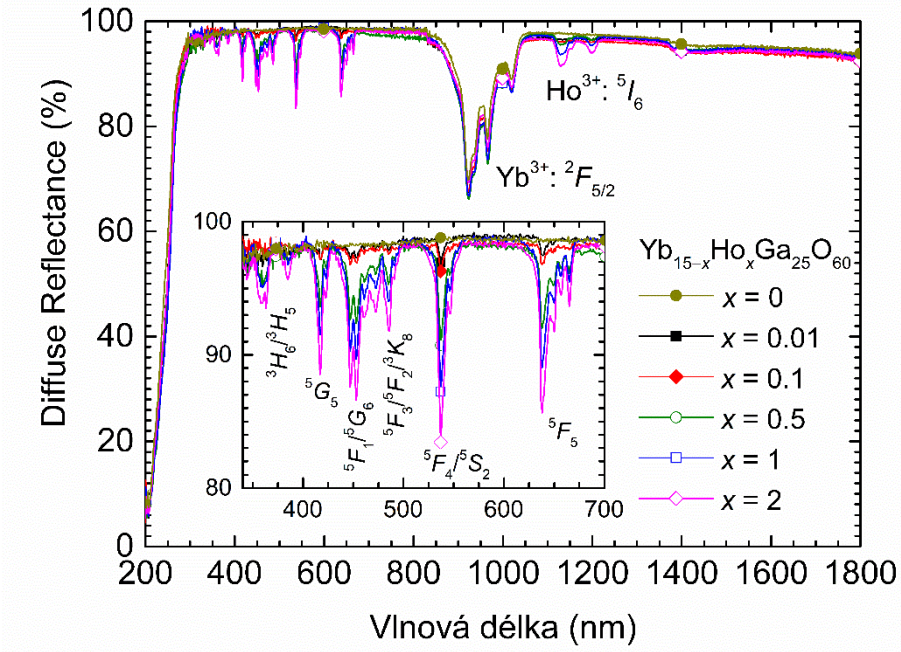

Fig. 12. Diffuse reflectance spectra of $Yb_{15-x}Ho_xGa_{25}O_{60}$ nanocrystalline garnets. Inset shows detail of the spectra in the 340–700 nm region.

Fig. 13 presents the Stokes emission spectra in the 1050–1350 nm region of prepared $Yb_{15-x}Ho_xGa_{25}O_{60}$ nanocrystalline garnets. The origin of these emission spectra is from the Ho^{3+}: $^5I_6 \rightarrow {}^5I_8$ electronic transition. The integrated PL intensity non-linearly increases from $x = 0.01$ up to $x = 1$, as is shown in the inset of Fig. 13. The decrease of integrated PL intensity of the $Yb_{13}Ho_2Ga_{25}O_{60}$ sample is assigned to the concentration quenching effect [41, 42]. Nevertheless, the relatively high value of integrated PL intensity the $Yb_{13}Ho_2Ga_{25}O_{60}$ sample suggests efficient pumping of the Ho^{3+}: $^5I_6$ level even at the high doping content.

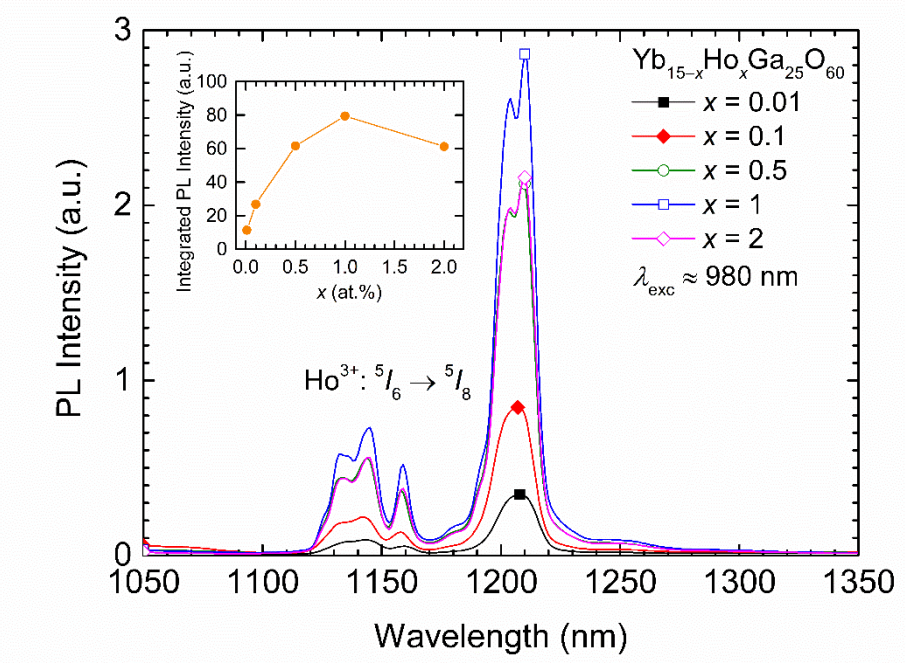

Fig. 13. Stokes Ho^{3+}: $^5I_6 \rightarrow {}^5I_8$ emission spectra of $Yb_{15-x}Ho_xGa_{25}O_{60}$ nanocrystalline garnets. Inset shows the variation of integrated PL intensity with Ho^{3+} content. Measured at λ_{exc} ≈980 nm.

Fig. 14 shows the Stokes emission spectra in the 1800–2300 nm region of prepared $Yb_{15-x}Ho_xGa_{25}O_{60}$ nanocrystalline garnets. The Ho^{3+}: $^5I_7 \rightarrow {}^5I_8$ electronic transition is responsible for these observed emission spectra. The integrated PL intensity shows a maximum for the $Yb_{14.5}Ho_{0.5}Ga_{25}O_{60}$ sample, as can be seen in the inset of Fig. 14. A significant decrease of the integrated PL intensity for the $Yb_{14}Ho_1Ga_{25}O_{60}$ and $Yb_{13}Ho_2Ga_{25}O_{60}$ samples suggests more efficient depopulation of the Ho^{3+}: $^5I_7$ level compared with the Ho^{3+}: $^5I_6$ level.

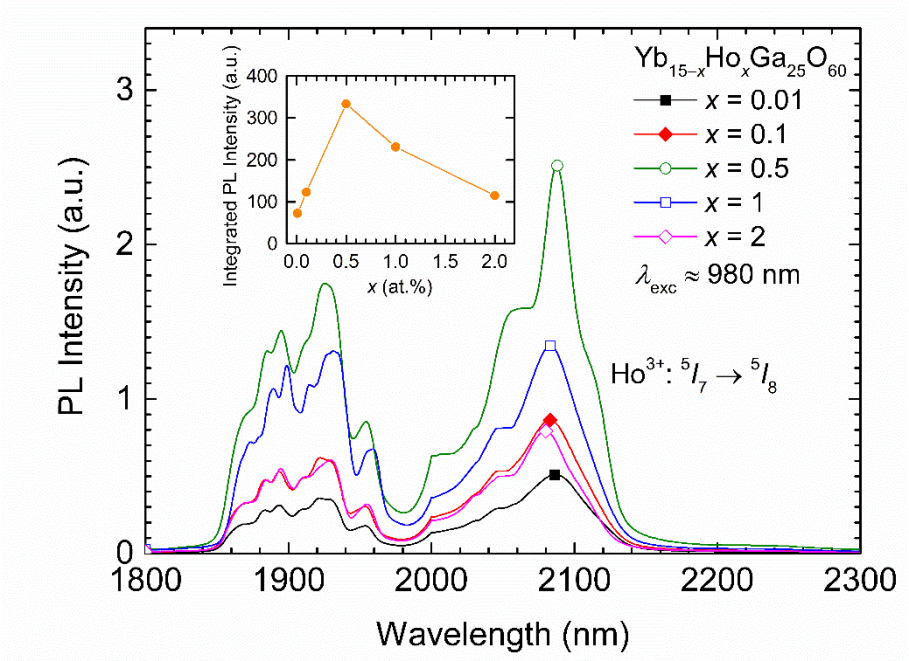

Fig. 14. Stokes Ho^{3+}: $^5I_7 \rightarrow {}^5I_8$ emission spectra of $Yb_{15-x}Ho_xGa_{25}O_{60}$ nanocrystalline garnets. Inset shows the variation of integrated PL intensity with Ho^{3+} content. Measured at λ_{exc} ≈980 nm.

Fig. 15 presents the anti-Stokes emission (upconversion) spectra in the 450–800 nm region of prepared $Yb_{15-x}Ho_xGa_{25}O_{60}$ nanocrystalline garnets. There are three types of the anti-Stokes emission bands. The relatively intense emission bands in "green" region (λ_{em} ≈530–570 nm) come from the Ho^{3+}: $^5F_4/^5S_2 \rightarrow {}^5I_8$ electronic transition. The relatively intense emission bands in "red" region (λ_{em} ≈630–700 nm) come from the Ho^{3+}: $^5F_5 \rightarrow {}^5I_8$ electronic transition. A significantly less intense emission bands in the 740–770 nm region (which are shown enlarged in the inset of Fig. 15) come from the Ho^{3+}: $^5F_4/^5S_2 \rightarrow {}^5I_7$ electronic transition. The highest photoluminescence instensity was detected here in the $Yb_{14.9}Ho_{0.1}Ga_{25}O_{60}$ sample. The efficient depopulation of the Ho^{3+}: $^5F_4/^5S_2$ and $^5F_5$ energy levels at $x > 0.1$ in the $Yb_{15-x}Ho_xGa_{25}O_{60}$ nanocrystalline garnets will be further discussed.

Fig. 16 shows the CIE 1931 chromaticity diagram of the observed anti-Stokes emission in $Yb_{15-x}Ho_xGa_{25}O_{60}$ nanocrystalline garnets. According to the observed diagram, the perceived color region changes from yellow to green as the Ho^{3+} concentration increases.

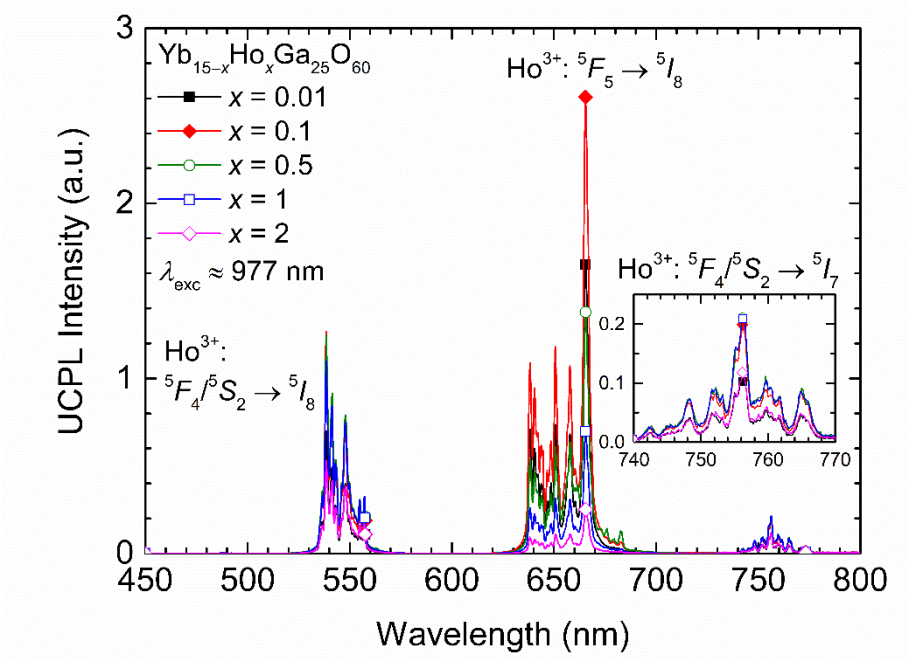

Fig. 15. Anti-Stokes emission spectra of $Yb_{15-x}Ho_xGa_{25}O_{60}$ nanocrystalline garnets. Inset shows detail of the spectra in the 740–770 nm region. Measured at λ_{exc} ≈977 nm.

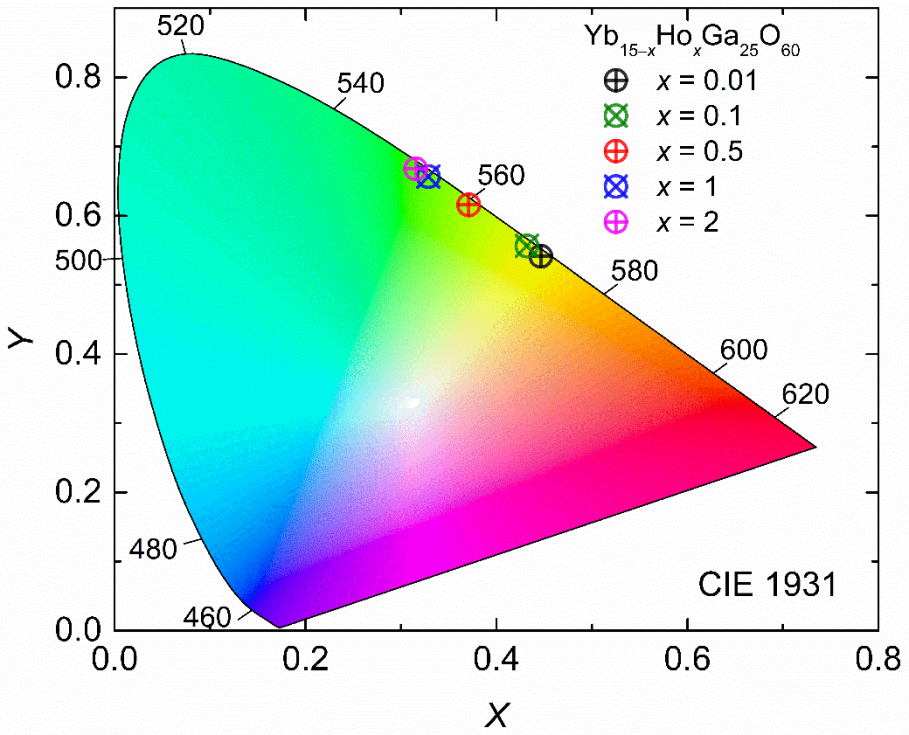

Fig. 16. CIE 1931 chromaticity diagram of the anti-Stokes emission in $Yb_{15-x}Ho_xGa_{25}O_{60}$ nanocrystalline garnets.

Tab. 4 lists the determined lifetime values of radiative transitions observed in $Yb_{15-x}Ho_xGa_{25}O_{60}$ nanocrystalline garnets. The single lifetime component $\tau(^5I_6)$ corresponds to the Ho^{3+}: $^5I_6 \rightarrow {}^5I_8$ transition. The $\tau(^5I_6)$ is gradually and slightly increased with increasing Ho^{3+} concentration from ≈245 μs ($Yb_{14.99}Ho_{0.01}Ga_{25}O_{60}$ sample) to

≈272 μs ($Yb_{13}Ho_2Ga_{25}O_{60}$ sample). This suggests efficient population of the Ho^{3+}: $^5I_6$ level by CR processes [52–54], which will be further discussed.

Both the short lifetime component $\tau_1(^5I_7)$ and the long lifetime component $\tau_2(^5I_7)$ show same trend with increasing Ho^{3+} content and come from the Ho^{3+}: $^5I_7 \rightarrow {}^5I_8$ transition. The average lifetime $<\tau>(^5I_7)$ shows same trend as well therefore. The $<\tau>(^5I_7)$ increases from ≈16.90 ms ($Yb_{14.99}Ho_{0.01}Ga_{25}O_{60}$ sample) to ≈17.84 ms ($Yb_{14.9}Ho_{0.1}Ga_{25}O_{60}$ sample), which may be caused by a radiation trapping effect [43]. The following decrease of $<\tau>(^5I_7)$ up to ≈2.44 ms ($Yb_{13}Ho_2Ga_{25}O_{60}$ sample) is mainly caused by CR processes [52–54] and by concentration quenching effect [41, 42].

The single lifetime component $\tau_{Yb}(^2F_{5/2})$ was detected only in the $Yb_{14.99}Ho_{0.01}Ga_{25}O_{60}$ and $Yb_{14.9}Ho_{0.1}Ga_{25}O_{60}$ samples with value of only ≈10 μs. In the $Yb_{15-x}Ho_xGa_{25}O_{60}$ samples with $x > 0.1$ the $\tau_{Yb}(^2F_{5/2})$ decreases bellow the detection limit. Nevertheless, such a low values of $\tau_{Yb}(^2F_{5/2})$ in the $Yb_{15-x}Ho_xGa_{25}O_{60}$ samples are caused by concentration quenching effect [41, 42] and by high efficiency of the $Yb^{3+} \rightarrow Ho^{3+}$ energy transfer process.

The two lifetime components $\tau_3(^5F_4/^5S_2)$ and $\tau_4(^5F_4/^5S_2)$ were determined in the $Yb_{14.99}Ho_{0.01}Ga_{25}O_{60}$ and $Yb_{14.9}Ho_{0.1}Ga_{25}O_{60}$ samples. However, the short lifetime component $\tau_3(^5F_4/^5S_2)$ decreases bellow the detection limit with $x > 0.1$ in the $Yb_{15-x}Ho_xGa_{25}O_{60}$ samples, the long lifetime component $\tau_4(^5F_4/^5S_2)$ gradually and slightly increases with increasing Ho^{3+} content. The origin of this phenomenon is probably more complex. Nevertheless, the increase of the long lifetime component $\tau_4(^5F_4/^5S_2)$ may be caused by a presence of EBT process depopulating the Ho^{3+}: $^5F_4/^5S_2$ levels, since with increasing Ho^{3+} content the Yb^{3+} content decreases and therefore the efficiency of the EBT process decreases [50, 52, 55, 56].

Tab. 4. Lifetime values of the Stokes emission Ho^{3+}: $^5I_6 \rightarrow {}^5I_8$ $\{\tau(^5I_6)\}$, Stokes emission Ho^{3+}: $^5I_7 \rightarrow {}^5I_8$ $\{\tau_1(^5I_7)$ and $\tau_2(^5I_7)\}$, Stokes emission Yb^{3+}: $^2F_{5/2} \rightarrow {}^2F_{7/2}$ $\{\tau_{Yb}(^2F_{5/2})\}$ and anti-Stokes emission Ho^{3+}: $^5F_4/^5S_2 \rightarrow {}^5I_8$ $\{\tau_3(^5F_4/^5S_2)$ and $\tau_4(^5F_4/^5S_2)\}$. $<\tau>(^5I_7)$ is the average lifetime of the Stokes emission Ho^{3+}: $^5I_7 \rightarrow {}^5I_8$.

x (at.%)	τ ($^5I_6$) (μs)	τ_1 ($^5I_7$) (ms)	τ_2 ($^5I_7$) (ms)	$<\tau>$ ($^5I_7$) (ms)	τ_{Yb} ($^2F_{5/2}$) (μs)	τ_3 ($^5F_4/^5S_2$) (μs)	τ_4 ($^5F_4/^5S_2$) (μs)
0.01	245±1	6.38±0.04	18.11±0.02	16.90±0.1	10±1	12±1	43±1
0.1	255±1	6.91±0.02	19.26±0.01	17.84±0.1	10±1	14±1	52±1
0.5	257±1	3.33±0.01	10.30±0.01	9.08±0.1	–	–	53±1
1	270±1	1.96±0.01	5.85±0.01	5.04±0.1	–	–	58±1
2	272±1	1.21±0.01	3.13±0.01	2.44±0.1	–	–	60±1

4.3.1. Photoluminescence mechanism in Ho^{3+}-doped $Yb_3Ga_5O_{12}$ nanocrystals

Fig. 17 presents the proposed photoluminescence mechanism in $Yb_{15-x}Ho_xGa_{25}O_{60}$ nanocrystalline garnets using λ_{exc} ≈980 nm. Firstly, the GSA process at Yb^{3+} ion occurs: Yb^{3+}: $^2F_{7/2} \rightarrow {}^2F_{5/2}$. The GSA process at Ho^{3+} ion cannot occur [52, 54] and the ESA process at Ho^{3+} ion will play a negligible role due to a high Yb^{3+}/Ho^{3+} content in all

studied samples. The GSA process leads to the ETU0 process: Yb^{3+}: $^2F_{5/2}$ + Ho^{3+}: $^5I_8$ → Yb^{3+}: $^2F_{7/2}$ + Ho^{3+}: $^5I_6$. Absorption of another photon by the Yb^{3+} is followed by the ETU1 process: Yb^{3+}: $^2F_{5/2}$ + Ho^{3+}: $^5I_6$ → Yb^{3+}: $^2F_{7/2}$ + Ho^{3+}: $^5F_4/^5S_2$. The radiative transition Ho^{3+}: $^5F_4/^5S_2$ → $^5I_8$ provides the observed anti-Stokes emission in "green" region. The radiative transition Ho^{3+}: $^5F_4/^5S_2$ → $^5I_7$ provides a much weaker "755 nm" emission. The emission in "red" region comes from the radiative transition Ho^{3+}: $^5F_5$ → $^5I_8$. At the Ho^{3+}: $^5I_6$ level, part of the electrons undergoes the Ho^{3+}: $^5I_6$ → $^5I_8$ radiative transition which is observed as the Stokes emission spectra at ≈1.2 μm. Another part of the electrons is depopulated by the MPR process to the lower-lying $^5I_7$ level. The radiative transition Ho^{3+}: $^5I_7$ → $^5I_8$ is observed at ≈2 μm. Nevertheless, part of electrons at the Ho^{3+}: $^5I_7$ level undergoes the ETU2 process: Yb^{3+}: $^2F_{5/2}$ + Ho^{3+}: $^5I_7$ → Yb^{3+}: $^2F_{7/2}$ + Ho^{3+}: $^5F_5$. The efficient population of the Ho^{3+}: $^5I_6$ level is provided by a presence of following CR and EBT processes. The CR1 process between pairs of Ho^{3+} ions is following: $^5F_4/^5S_2$ + $^5I_7$ → $^5F_5$ + $^5I_6$ [52, 54]. The CR2 process between pairs of Ho^{3+} ions is following: $^5I_7$ + $^5I_7$ → $^5I_8$ + $^5I_6$ [53]. The EBT process between Yb^{3+} and Ho^{3+} occurs as follows: Ho^{3+}: $^5F_4/^5S_2$ + Yb^{3+}: $^2F_{7/2}$ → Ho^{3+}: $^5I_6$ + Yb^{3+}: $^2F_{5/2}$ [52, 55, 56].

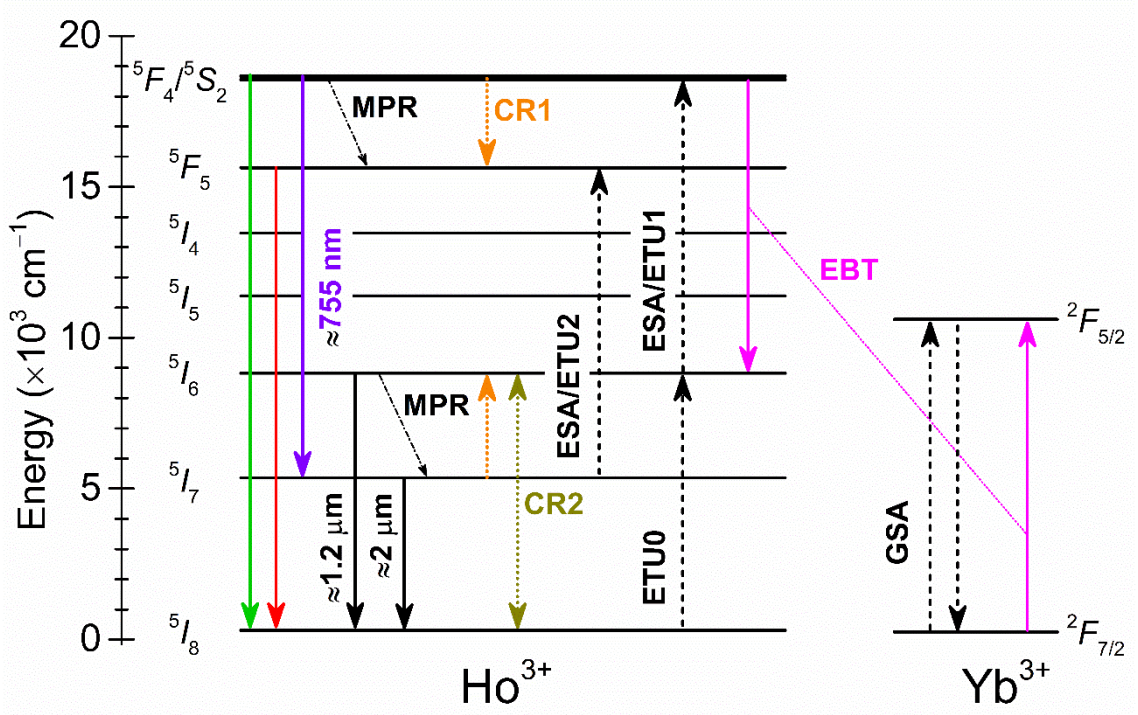

Fig. 17. Proposed photoluminescence mechanism in $Yb_{15-x}Ho_xGa_{25}O_{60}$ nanocrystalline garnets using λ_{exc} ≈980 nm.

5. CONCLUSION

Within the submitted dissertation thesis, the nanocrystalline oxides with the composition $Yb_{15-x}Er_xGa_{25}O_{60}$ and $Yb_{15-x}Ho_xGa_{25}O_{60}$ (x = 0, 0.01, 0.1, 0.5, 1 and 2 at.%) were prepared by the sol-gel combustion technique using citric acid. X-ray diffraction analysis confirmed the single-phase nature of all prepared nanocrystals corresponding to the cubic $Yb_3Ga_5O_{12}$ garnet structure. The presence of structural units of YbO_8 dodecahedrons, GaO_6 octahedrons and GaO_4 tetrahedrons was confirmed by attenuated total reflectance-Fourier transform infrared spectroscopy. Since the mean crystallite size of the prepared samples ranges from ≈27 to ≈37 nm, the samples can be classified as nanocrystalline oxides which was also proved by scanning electron microscopy. The chemical composition of the nanocrystalline garnets determined using energy-dispersive X-ray spectrometry corresponds to the theoretical composition. Analyzing the diffuse reflectance spectra, one can say that all the studied nanocrystalline garnets show high optical reflectivity from the visible up to a part of the near-infrared region. The absorption bands of present Er^{3+}/Ho^{3+} and Yb^{3+} ions originated from the 4f ↔ 4f electronic transitions are well defined in the diffuse reflectance spectra. A broad and intense absorption band between ≈850 to ≈1050 nm corresponds to high Yb^{3+} content in all studied samples and makes the doped samples suitable for efficient pumping by the 980nm laser.

The intense Stokes and anti-Stokes emission bands were observed in the $Yb_{15-x}Er_xGa_{25}O_{60}$ nanocrystalline garnets. The Stokes emission bands in the ≈1450–1650 nm region come from the Er^{3+}: $^4I_{13/2} \rightarrow {}^4I_{15/2}$ electronic transition. The anti-Stokes emission bands in the visible region show intense bands in "red" region originating from the Er^{3+}: $^4F_{9/2} \rightarrow {}^4I_{15/2}$ electronic transition. The emission bands in "green" region originating from the Er^{3+}: $^4F_{7/2}/^2H_{11/2}/^4S_{3/2} \rightarrow {}^4I_{15/2}$ electronic transition were significantly less intense. The observed anti-Stokes emission therefore occurs in a deep red region. The lifetime values of observed radiative transitions were determined and the photoluminescence mechanism was proposed. The energy transfer $Yb^{3+} \rightarrow Er^{3+}$ and the energy back transfer $Er^{3+} \rightarrow Yb^{3+}$ play a dominant role in the observed photoluminescence properties of all $Yb_{15-x}Er_xGa_{25}O_{60}$ nanocrystalline garnets. In the $Yb_{15-x}Er_xGa_{25}O_{60}$ nanocrystalline garnets with $x > 0.01$, the cross-relaxation $Er^{3+} \leftrightarrow Er^{3+}$ processes further contribute.

The intense Stokes and anti-Stokes emission bands were also observed in the $Yb_{15-x}Ho_xGa_{25}O_{60}$ series. The Stokes emission bands in the ≈1050–1350 nm region come from the Ho^{3+}: $^5I_6 \rightarrow {}^5I_8$ electronic transition. The Stokes emission bands in the ≈1800–2300 nm region come from the Ho^{3+}: $^5I_7 \rightarrow {}^5I_8$ electronic transition. The anti-Stokes emission bands in the visible region show intense bands in "green" region originating from the Ho^{3+}: $^5F_4/^5S_2 \rightarrow {}^5I_8$ electronic transition. The intense anti-Stokes emission bands are also in "red" region which come from the Ho^{3+}: $^5F_5 \rightarrow {}^5I_8$ electronic transition. The emission bands in "755 nm" region originating from the Ho^{3+}: $^5F_4/^5S_2 \rightarrow {}^5I_7$ electronic transition were significantly less intense. The observed emission color of the anti-Stokes emission can be easily tuned changing the Ho^{3+} content. The lifetime values of observed radiative transitions were also determined and the photoluminescence mechanism was proposed as well. The energy transfer $Yb^{3+} \rightarrow Ho^{3+}$ and the energy back transfer $Ho^{3+} \rightarrow Yb^{3+}$ play a dominant role here in the observed photoluminescence properties of all $Yb_{15-x}Ho_xGa_{25}O_{60}$ nanocrystals. With $x > 0.01$ in the $Yb_{15-x}Ho_xGa_{25}O_{60}$ series, the cross-relaxation $Ho^{3+} \leftrightarrow Ho^{3+}$ processes further occur.

LIST OF REFERENCES

[1] G.-M. Chow, N.I. Noskova, Nanostructured Materials: Science & Technology. American Society for Engineering Education, Washington DC (1998), ISBN 0-7923-5071-5.

[2] G. Wang, Q. Peng, Y. Li, Lanthanide-Doped Nanocrystals: Synthesis, Optical-Magnetic Properties, and Applications, Acc. Chem. Res. 44 (2011) 322–332, https://doi.org/10.1021/ar100129p.

[3] E.S. Grew, A.J. Locock, S.J. Mills, I.O. Galuskina, E.V. Galuskin, U. Hålenius, Nomenclature of the garnet supergroup, Am. Mineral. 98 (2013) 785–811, https://doi.org/10.2138/am.2013.4201.

[4] J.E. Geusic, H.M. Marcos, L.G. Van Uitert, Laser oscillations in Nd-doped yttrium aluminum, yttrium gallium and gadolinium garnets, Appl. Phys. Lett. 4 (1964) 182–184, https://doi.org/10.1063/1.1753928.

[5] L. Mezeix, D.J. Green, Comparison of the mechanical properties of single crystal and polycrystalline yttrium aluminum garnet, Int. J. Appl. Ceram. Technol. 3 (2006) 166–176, https://doi.org/10.1111/j.1744-7402.2006.02068.x.

[6] J. Li, Y. Wu, Y. Pan, W. Liu, L. Huang, J. Guo, Fabrication, microstructure and properties of highly transparent Nd:YAG laser ceramics, Opt. Mater. 31 (2008) 6–17, https://doi.org/10.1016/j.optmat.2007.12.014.

[7] Z. You, Y. Wang, J. Xu, Z. Zhu, J. Li, C. Tu, Diode-end-pumped midinfrared multiwavelength Er:Pr:GGG laser, IEEE Photon. Technol. Lett. 26 (2014) 667–670, https://doi.org/10.1109/LPT.2014.2302837.

[8] G.A. Novak, G.V. Gibbs, The Crystal Chemistry of the Silicate Garnets, Am. Mineral. 56 (1971) 791–825.

[9] A. Bosenick, M.T. Dove, C.A. Geiger, Simulation studies on the pyrope-grossular garnet solid solution, Phys. Chem. Miner. 27 (2000) 398–418, https://doi.org/10.1007/s002690000088.

[10] V. Monteseguro, P. Rodríguez-Hernández, V. Lavín, F.J. Manjón, A. Muñoz, Electronic and elastic properties of yttrium gallium garnet under pressure from ab initio studies, J. Appl. Phys. 113 (2013) 183505, https://doi.org/10.1063/1.4804133.

[11] Z. Song, D. Zhou, Q. Liu, Tolerance factor and phase stability of the garnet structure, Acta Cryst. C 75 (2019) 1353–1358, https://doi.org/10.1107/S2053229619011975.

[12] Z. Xia, A. Meijerink, Ce^{3+}-Doped garnet phosphors: composition modification, luminescence properties and applications, Chem. Soc. Rev. 46 (2017) 275–299, https://doi.org/10.1039/c6cs00551a.

[13] F. Han, Y. Zhu, X. He, Y. Mo, C. Wang, Electrochemical Stability of $Li_{10}GeP_2S_{12}$ and $Li_7La_3Zr_2O_{12}$ Solid Electrolytes, Adv. Energy Mater. 6 (2016) 1501590, https://doi.org/10.1002/aenm.201501590.

[14] M. Klank, O. Hagedorn, M. Shamonin, H. Dötsch, Sensitive magneto-optical sensors for visualization of magnetic fields using garnet films of specific orientations, J. Appl. Phys. 92 (2002) 6484–6488, https://doi.org/10.1063/1.1516839.

[15] J. Xu, D. Murata, J. Ueda, S. Tanabe, Near-infrared long persistent luminescence of Er^{3+} in garnet for the third bio-imaging window, J. Mater. Chem. C 4 (2016) 11096–11103, https://doi.org/10.1039/c6tc04027f.

[16] M. Guillot, H. Le Gall, J. Ostorero, M. Artinian, A. Marchand, Faraday rotation in single-crystal ytterbium gallium garnet, J. Appl. Phys. 61 (1987) 3265–3267,

https://doi.org/10.1063/1.338876.
[17] K. Królas, M. Rams, A. Forget, J. Wojtkowska, Paramagnetic fluctuations in $Yb_3Ga_5O_{12}$ investigated with ^{172}Yb PAC probe, Hyperfine Interact. 120 (1999) 231–235, https://doi.org/10.1023/A:1017071206102.
[18] J.A. Hodges, P. Bonville, M. Rams, K. Królas, Low temperature spin fluctuations in geometrically frustrated $Yb_3Ga_5O_{12}$, J. Phys. Condens. Matter. 15 (2003) 4631, https://doi.org/10.1088/0953-8984/15/26/313.
[19] J.C. Kim, M.-H. Kim, S. Nahm, J.-H. Paik, J.-H. Kim, H.-J. Lee, Microwave dielectric properties of $Re_3Ga_5O_{12}$ (Re: Nd, Sm, Eu, Dy and Yb) ceramics and effect of TiO_2 on the microwave dielectric properties of $Sm_3Ga_5O_{12}$ ceramics, J. Eur. Ceram. Soc. 27 (2007) 2865–2870, https://doi.org/10.1016/j.jeurceramsoc.2006.11.066.
[20] A. Shibuya, T. Shibuya, T. Manako, Thermal radiation properties of porous rare-earth garnet ceramics, J. Ceram. Soc. Jpn. 126 (2018) 447–451, http://doi.org/10.2109/jcersj2.18021.
[21] V. Singh, G. Sivaramaiah, J.L. Rao, N. Singh, M.S. Pathak, H.D. Jirimali, P.K. Singh, A.K. Srivastava, S.J. Dhoble, M. Mohapatra, Cr^{3+}-Doped $Yb_3Ga_5O_{12}$ Nanophosphor: Synthesis, Optical, EPR, Studies, J. Electron. Mater. 45 (2016) 4076–4082, https://doi.org/10.1007/s11664-016-4575-5.
[22] A. Dulda, 805 nm Mediated Upconversion Luminescence Properties of $Yb_3Ga_5O_{12}$:Ln (Er^{3+}/Nd^{3+}) Nanoparticles, NANO: Brief Reports and Reviews 11 (2016) 1650098, https://doi.org/10.1142/S1793292016500983.
[23] V. Buissette, D. Giaume, T. Gacoin, J.-P. Boilot, Aqueous routes to lanthanide-doped oxide nanophosphors, J. Mater. Chem. 16 (2006) 529–539, https://doi.org/10.1039/B508656F.
[24] N. Abid, A.M. Khan, S. Shujait, K. Chaudhary, M. Ikram, M. Imran, J. Haider, M. Khan, Q. Khan, M. Maqbool, Synthesis of nanomaterials using various top-down and bottom-up approaches, influencing factors, advantages, and disadvantages: A review, Adv. Colloid Interface Sci. 300 (2022) 102597, https://doi.org/10.1016/j.cis.2021.102597.
[25] A.E. Danks, S.R. Hall, Z. Schnepp, The evolution of 'sol–gel' chemistry as a technique for materials synthesis, Mater. Horiz. 3 (2016) 91–112, https://doi.org/10.1039/c5mh00260e.
[26] D. Ouyang, Z. Huang, W.C.H. Choy, Solution-Processed Metal Oxide Nanocrystals as Carrier Transport Layers in Organic and Perovskite Solar Cells, Adv. Funct. Mater. 29 (2019) 1804660, https://doi.org/10.1002/adfm.201804660.
[27] J. Singh, Optical Properties of Condensed Matter and Applications. Wiley, Hoboken (2006), ISBN 0-470-02192-6.
[28] C.R. Ronda, Luminescence From Theory to Applications. Wiley, Weinheim (2008), ISBN 978-3-527-31402-7.
[29] I. Pelant, J. Valenta, Luminiscenční spektroskopie. Academia, Praha (2006), ISBN 80-200-1447-0.
[30] H. Yersin, Transition Metal and Rare Earth Compounds. Springer, Berlin (2001), ISBN 978-3-540-67976-9.
[31] I.K. Battisha, Visible Up-Conversion Luminescence in Ho^{3+}: $BaTiO_3$ Nano-Crystals Prepared by Sol Gel Technique, J. Sol-Gel Sci. Technol. 30 (2004) 163–172, https://doi.org/10.1023/B:JSST.0000039501.22116.86.
[32] A. Shalav, B.S. Richards, M.A. Green, Luminescent layers for enhanced silicon

solar cell performance: Up-conversion, Sol. Energy Mater. Sol. Cells 91 (2007) 829–842, https://doi.org/10.1016/j.solmat.2007.02.007.
[33] Z. Liu, Z. Li, J. Liu, S. Gu, Q. Yuan, J. Ren, X. Qu, Long-circulating Er^{3+}-doped Yb_2O_3 up-conversion nanoparticle as an in vivo X-Ray CT imaging contrast agent, Biomaterials 33 (2012) 6748–6757, https://doi.org/10.1016/j.biomaterials.2012.06.033.
[34] A. Patra, C.S. Friend, R. Kapoor, P.N. Prasad, Upconversion in Er^{3+}:ZrO_2 Nanocrystals, J. Phys. Chem. B 106 (2002) 1909–1912, https://doi.org/10.1021/jp013576z.
[35] P. Scherrer, Bestimmung der Größe und der inneren Struktur von Kolloidteilchen mittels Röntgenstrahlen, Nachrichten von der Gesellschaft der Wissenschaften zu Göttingen, Mathematisch Physikalische Klasse 1918 (1918) 98–100.
[36] N.T. McDevitt, Infrared Lattice Spectra of Rare-Earth Aluminum, Gallium, and Iron Garnets, J. Opt. Soc. Am. 59 (1969) 1240–1244, https://doi.org/10.1364/JOSA.59.001240.
[37] S.M. Elhamali, N.B. Ibrahim, S. Radiman, Structural, optical and magnetic properties of YIG and TbErIG nanofilms prepared using a sol-gel method, Mater. Res. Bull. 112 (2019) 66–76, https://doi.org/10.1016/j.materresbull.2018.12.005.
[38] V. Venkatramu, M. Giarola, G. Mariotto, S. Enzo, S. Polizzi, C.K. Jayasankar, F. Piccinelli, M. Bettinelli, A. Speghini, Nanocrystalline lanthanide-doped $Lu_3Ga_5O_{12}$ garnets: interesting materials for light-emitting devices, Nanotechnology 21 (2010) 175703, http://dx.doi.org/10.1088/0957-4484/21/17/175703.
[39] M.C. Saine, E. Husson, H. Brusset, A. Cerez, Etude vibrationnelle d'aluminates et de gallates de terres rares—III. Aluminates et gallates de structure grenat, Spectrochim. Acta A 38 (1982) 25–29, https://doi.org/10.1016/0584-8539(82)80173-6.
[40] A.M. Hofmeister, K.R. Campbell, Infrared spectroscopy of yttrium aluminum, yttrium gallium, and yttrium iron garnets, J. Appl. Phys. 72 (1992) 638–646, https://doi.org/10.1063/1.351846.
[41] D.L. Dexter, J.H. Schulman, Theory of Concentration Quenching in Inorganic Phosphors, J. Chem. Phys. 22 (1954) 1063–1070, https://doi.org/10.1063/1.1740265.
[42] A.D. Sontakke, K. Biswas, A.K. Mandal, K. Annapurna, Concentration quenched luminescence and energy transfer analysis of Nd^{3+} ion doped Ba-Al-metaphosphate laser glasses, Appl. Phys. B 101 (2010) 235–244, https://doi.org/10.1007/s00340-010-4010-1.
[43] F. Auzel, G. Baldacchini, L. Laversenne, G. Boulon, Radiation trapping and self-quenching analysis in Yb^{3+}, Er^{3+}, and Ho^{3+} doped Y_2O_3, Opt. Mater. 24 (2003) 103–109, https://doi.org/10.1016/S0925-3467(03)00112-5.
[44] J.P. Wittke, I. Ladany, P.N. Yocom, Y_2O_3 : Yb : Er-New Red-Emitting Infrared-Excited Phosphor, J. Appl. Phys. 43 (1972) 595–600, https://doi.org/10.1063/1.1661163.
[45] J. Zhao, Y. Sun, X. Kong, L. Tian, Y. Wang, L. Tu, J. Zhao, H. Zhang, Controlled Synthesis, Formation Mechanism, and Great Enhancement of Red Upconversion Luminescence of $NaYF_4$:Yb^{3+}, Er^{3+} Nanocrystals/Submicroplates at Low Doping Level, J. Phys. Chem. B 112 (2008) 15666–15672, https://doi.org/10.1021/jp805567k.
[46] A. Lupei, V. Lupei, S. Georgescu, I. Ursu, V.I. Zhekov, T.M. Murina, A.M. Prokhorov, Many-body energy-transfer processes between Er^{3+} ions in yttrium aluminum garnet, Phys. Rev. B 41 (1990) 10923–10932, https://doi.org/10.1103/PhysRevB.41.10923.

[47] F.E. Auzel, Materials and devices using double-pumped-phosphors with energy transfer, Proceedings of the IEEE 61 (1973) 758–786, https://doi.org/10.1109/PROC.1973.9155.
[48] J. Liu, H. Deng, Z. Huang, Y. Zhang, D. Chen, Y. Shao, Phonon-assisted energy back transfer-induced multicolor upconversion emission of Gd_2O_3:Yb^{3+}/Er^{3+} nanoparticles under near-infrared excitation, Phys. Chem. Chem. Phys. 17 (2015) 15412–15418, https://doi.org/10.1039/c5cp01632k.
[49] J. Chen, J.J. Guo, Y.H. Chen, X.S. Peng, G.A. Ashraf, H. Guo, Up-conversion properties of $Ba_3Lu_2Zn_5O_{11}$:Yb^{3+},Er^{3+} phosphors for optical thermometer based on FIR technique, J. Lumin. 238 (2021) 118294, https://doi.org/10.1016/j.jlumin.2021.118294.
[50] A. Li, D. Xu, Y. Zhang, H. Lin, S. Yang, Z. Chen, Y. Shao, Upconversion Luminescence and Energy-Transfer Mechanism of $NaGd(MoO_4)_2$: Yb^{3+}/Er^{3+} Microcrystals, J. Am. Ceram. Soc. 99 (2016) 1657–1663, https://doi.org/10.1111/jace.14141.
[51] F. Vetrone, J.C. Boyer, J.A. Capobianco, Significance of Yb^{3+} concentration on the upconversion mechanisms in codoped Y_2O_3:Er^{3+}, Yb^{3+} nanocrystals, J. Appl. Phys. 96 (2004) 661–667, https://doi.org/10.1063/1.1739523.
[52] N.M. Sangeetha, F.C.J.M. van Veggel, Lanthanum Silicate and Lanthanum Zirconate Nanoparticles Co-Doped with Ho^{3+} and Yb^{3+}: Matrix-Dependent Red and Green Upconversion Emissions, J. Phys. Chem. C 113 (2009) 14702–14707, https://doi.org/10.1021/jp904516s.
[53] R. Cao, Y. Lu, Y. Tian, F. Huang, Y. Guo, S. Xu, J. Zhang, 2 μm emission properties and nonresonant energy transfer of Er^{3+} and Ho^{3+} codoped silicate glasses, Sci. Rep. 6 (2016) 37873, https://doi.org/10.1038/srep37873.
[54] X. Chai, J. Li, X. Wang, Y. Li, X. Yao, Upconversion luminescence and temperature-sensing properties of Ho^{3+}/Yb^{3+}-codoped $ZnWO_4$ phosphors based on fluorescence intensity ratios, RSC Adv. 7 (2017) 40046–40052, https://doi.org/10.1039/C7RA05846B.
[55] X.X. Zhang, P. Hong, M. Bass, B.H.T. Chai, Ho^{3+} to Yb^{3+} back transfer and thermal quenching of upconversion green emission in fluoride crystals, Appl. Phys. Lett. 63 (1993) 2606–2608, https://doi.org/10.1063/1.110445.
[56] X. Wei, Y. Li, X. Cheng, Y. Chen, M. Yin, Strong dependence of upconversion luminescence on doping concentration in holmium and ytterbium co-doped Y_2O_3 phosphor, J. Rare Earths 29 (2011) 536–539, https://doi.org/10.1016/S1002-0721(10)60493-0.

LIST OF STUDENTS' PUBLISHED WORKS

[1] T. Netolicky, L. Benes, K. Melanova, S. Slang, J. Oswald, T. Wagner, Near-infrared emission in Ho^{3+}-doped $Yb_3Ga_5O_{12}$ garnet nanocrystals, J. Lumin. 251 (2022) 119230, https://doi.org/10.1016/j.jlumin.2022.119230.

[2] T. Netolicky, L. Strizik, L. Benes, K. Melanova, S. Slang, T. Wagner, Deep red upconversion photoluminescence in Er^{3+}-doped $Yb_3Ga_5O_{12}$ nanocrystalline garnet, J. Am. Ceram. Soc. 105 (2022) 3391–3402, https://doi.org/10.1111/jace.18313.

LIST OF CONFERENCES AND INTERNSHIP

CONFERENCES:

[1] T. Netolicky, L. Benes, K. Melanova, S. Slang, J. Oswald, T. Wagner, Near-infrared emission and upconversion in nanocrystalline Er^{3+}/Ho^{3+}-doped $Yb_3Ga_5O_{12}$ garnet, Inorganic non-metallic materials seminar Praha (2023).

[2] T. Netolicky, L. Benes, K. Melanova, S. Slang, J. Oswald, T. Wagner, Near-infrared emission and upconversion in nanocrystalline Er^{3+}/Ho^{3+}-doped $Yb_3Ga_5O_{12}$ garnet, NANOCON Brno (2022) – Dr. Tasilo Prnka prize for the best author under 33.

[3] T. Netolicky, L. Strizik, T. Wagner, L. Benes, K. Melanova, S. Slang, Upconversion photoluminescence of nanocrystalline rare-earth ion doped $Yb_3Ga_5O_{12}$ (RE = Er^{3+}, Ho^{3+}), NANOCON Brno (2021).

[4] T. Netolicky, L. Strizik, T. Wagner, L. Benes, K. Melanova, S. Slang, Sol-gel synthesis and upconversion properties of nanocrystalline Er^{3+}-doped $Yb_3Ga_5O_{12}$, 14th International Conference on Solid State Chemistry Trenčín (2021).

[5] T. Netolicky, T. Wagner, L. Strizik, K. Melanova, S. Slang, Red upconversion emission of nanocrystalline Er^{3+}-doped $Yb_3Ga_5O_{12}$ prepared by sol-gel combustion synthesis, Inorganic non-metallic materials seminar Praha (2021).

INTERNSHIP:

The University of Sheffield, Department of Materials Science and Engineering, United Kingdom, topic: Synthesis and structure study of nanocrystalline ceramic oxides, 2 months (May 2 – July 1, 2022).